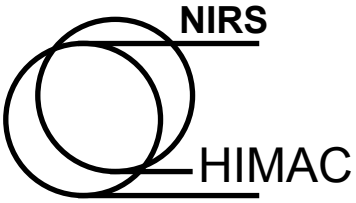

HIMAC-075

Design of APhF-IH Linac

for a Compact Medical Accelerator

Valery Kapin, Satoru Yamada, Yoshiyuki Iwata

December, 2003

National Institute of Radiological Sciences
9-1 Anagawa 4-chome, Inage-ku, Chiba 263-8555, JAPAN

Design of APhF-IH Linac for a Compact Medical Accelerator

Valery Kapin*, Satoru Yamada, Yoshiyuki Iwata

Department of Accelerator Physics and Engineering
National Institute of Radiological Sciences

4-9-1 Anagawa, Inage-ku, Chiba 263-8555, JAPAN

Abstract: The design of a small injection linac for a compact medical synchrotron is discussed. The linac design is based on interdigital H-type (IH) drift-tube structure with alternative phase focusing (APhF). A high acceleration rate and an absence of magnetic lenses inside drift-tubes reduce the cost and length of APhF-IH linac in comparison with HIMAC linac based on Alvarez structure with magnet quadrupoles inside drift-tubes. To reduce effects of emittance growth, the RFQ structure is used in front of the APhF linac. In such linac layout, the current transmission of a carbon beam can reach up to 90-100%. In this report, the basic parameters of whole linac are presented, while the design of APhF structure is considered in details.

Two reference designs of 4 MeV/u 200 MHz APhF linacs with different voltage distributions along the whole tank have been generated and analyzed numerically. For the first design, a constant voltage distribution along the tank is assumed. The total length of the structure is about 4.2 m. For the second design, a gradient type of voltage distribution is assumed. The total length of the second design is twice shorter (about 2.1 m). Both designs keep the same value of the maximum electric field on the drift-tube surfaces along the whole tanks. It is about 1.6 of the Kilpatrick limit.

The second design with a gradient-type of voltage distribution looks to be more attractive. A required voltage distribution can be realized in IH-tank. An example of gradient-voltage distribution calculated with Microwave Studio code is presented.

---

*On leave from Moscow Engineering Physics Institute;
e-mail: kapin@mail.ru

1. Introduction

More than 1,000 patients have been treated with carbon ions accelerated by a medical synchrotron HIMAC at National Institute of Radiological Sciences, NIRS [1]. The results of the clinical studies, the purposes of which are to confirm the effectiveness of the carbon therapy keeping side effects at extremely low levels, seem excellent [2]. However, HIMAC facility has a large size and is very expensive for a budget of local hospitals. Major activity of the Department of Accelerator Physics and Engineering at NIRS is concentrated on the developments of a small sized therapy system aiming to spread the carbon therapy in the whole country. A compact and reliable accelerator system is required to be developed for this purpose.

The compact medical accelerator consists of carbon synchrotron and injection linac. The injection linac is an important factor for the construction and operation cost of medical facility. In this report, design considerations and preliminary calculations for a small injection linac are presented. The linac consists of a 400 keV/u four-vane cavity with the radio-frequency quadrupole (RFQ) focusing and a 4 MeV/u interdigital H-type (IH) drift-tube (DT) cavity with an alterative phase focusing (APhF). Both structures operate at the RF frequency of 200 MHz. A similar linac layout has been recently considered at GSI, Germany [3].

In comparison with a classical heavy-ion linac consisting of RFQ and Alvarez-tank with magnet quadrupoles inside drift-tubes, the combination of RFQ with IH-APhF has a smaller size and provides an appropriate beam quality. A high acceleration rate and absence of magnetic lenses inside drift-tubes are the most attractive features of IH-APhF linac [3], which essentially reduce its length and cost. For example, HIMAC linac [4] with a conventional layout consists of the 0.8 MeV/u 7 m long RFQ and the 6 MeV/u 24 m long Alvarez tanks, and the GSI design of the 7 MeV/u injection linac consists of a short 0.3 MeV/u RFQ and the 4.3 m long IH-APhF structure.

However, a beam emittance growth due to coupling between radial and longitudinal motion is a main disadvantage of APhF-linac. To reduce effects of an emittance growth, it is favorable to accelerate short-bunched beams in APhF-linac. A high quality bunched beams can be delivered by a conventional RFQ structure located before an APhF-structure. In such linac layout, the beam current transmission from a carbon ion source to the synchrotron can reach up to 90-100%. Thus, the beam losses in the linac can be essentially diminished. It is important advantage of such linac layout, since carbon ion sources have limited beam currents.

In this report, the design of APhF-structure is considered in details. The design of RFQ structure is not presented here, since design technology of RFQ is well known and proved both theoretically and experimentally, including HIMAC RFQ [4].

It is known, that the focusing strength of APhF linac is inversely proportional to the particle energy. With a decrease of the focusing strength, a portion of stable particles (or the APhF acceptance) diminishes [5,6]. To compensate such drop of the focusing strength, the number of accelerating gaps in a focusing period, N_g should be increased. Such change of the focusing period is accompanied by a growth of beam emittance. An increasing the voltage between drift-tubes along the tank can provide an auxiliary way for the particular compensation of the focusing strength drop. A usage of such gradient-type of voltage distribution along the tank reduces a required range for a variation of N_g.

Two reference designs of APhF linacs with different voltage distributions along the whole tank have been generated and analyzed numerically. Both designs keep the same value of the maximum electric field on the drift-tube surfaces along the whole tanks. It is about 1.6 of the Kilpatrick limit. For the first design, a constant voltage distribution along the tank is assumed and the total length of structure is about 4.2 m. For the second design, a gradient type of voltage distribution is assumed and the total length of structure is twice less (about 2.1 m). The gradient-type of voltage distribution looks to be more attractive and can be realized in IH-tank. An example of gradient-voltage distribution calculated with Microwave Studio code is presented.

Another problem of APhF structures is a strong dependence of a beam quality on small drift-tube misalignments along structure and on fluctuations of the gap voltages about programmed values [3,7]. The effects of random errors in drift-tube positions and electrical fields in gaps can be evaluated analytically. Using formulae presented in Ref. [7], the level of permissible errors for the drift-tube displacements is about several 100 μm and for the fluctuations of the gap voltages is about 5-10 %. A careful technology for mechanical assembling and RF measuring can ensure these levels of precision. The more detailed study of these effects requires additional beam dynamics simulations and is not considered in this report.

2. Basic parameters of injection linac

Basic parameters of injection linac are presented in Table 1. The linac consists of RFQ tank and IH-APhF drift-tube structure both operating at the RF frequency of 200 MHz. The frequency is twice higher than one of the HIMAC linac in order to reduce tank sizes. The total length of linac is restricted by the value of 5 m. The length of 200 MHz 400 keV/u RFQ linac can be less than 1.5 m. For example, the length of the 400 keV/u RFQ linac presented in Ref. [8] for the GSI linac is 1.35 m. Hence, the length of APhF linac can not exceed 3-4 m.

In this paper, two options of APhF linac with different voltage distributions along the tank are considered. The first design assumes a constant voltage distribution along a whole tank, and second design assumes a gradient type of voltage distribution along the tank, while the gap voltage is proportional to the relative velocity of the synchronous particle, $U_g \propto \beta_s$. Figure 1 shows voltage distributions for the both cases.

The design of RF cavity should prevent RF electric breakdown. The maximum peak surface field E_S is expressed as $E_S = b \cdot E_{Kilpatrick}$ [9], where b is known as the bravery factor, and $E_{Kilpatrick}$ is known as the Kilpatrick limit. For our linac designs $b = 1.6$ is assumed. With $E_{Kilpatrick}$ =147 kV/cm at 200 MHz, the peak surface field E_S=236 kV/cm.

In order to keep the same voltage breakdown conditions along a whole structure, the gap length, l_g is kept to be a constant for the constant-voltage design and is proportional to the relative particle velocity, β_s for the gradient-voltage design. Figure 2 shows the distributions of the gap factor $\alpha_g = l_g / \beta_s \lambda$ along the structure, where λ is the wavelength.

To evaluate the surface field E_S on the drift-tube surfaces, the computer code POISSON [10] has been used. Figure 3 shows the calculation results for the first accelerating cell. The aperture radius a =5 mm, the internal and external radii of drift tube corners are equal to 2 mm and 4 mm, respectively. The maximal surface field is reached on the surface of the external corner of the drift-tube.

Some analytical approaches for a drift tube linac use the square-wave approximation for the gap field. The amplitude of square-wave is the ratio between the gap voltage and the gap length, $E_g = U_g / l_g$. For the first accelerating cell of our designs, the ratio between the maximum surface filed and amplitude of square-wave E_S / E_g is equal to 1.47.

For the first accelerating cells of both designs, E_g=158 kV/cm at the gap voltage U_g =173 kV and the gap length l_g =1.1 cm. The first design keeps constant values of U_g , l_g and, hence, E_g . However, the average value of the accelerating field $E_0 = 2E_g / \beta_s \lambda$ reduces from 79 kV/m to 25 kV/m, decreasing an acceleration rate at the exit end of the first design. The second design keeps constant values of E_g and E_0=79 kV/m along a whole structure, resulting in a shorter length of structure.

The energy gain ΔW_s in the RF gap is well approximated by the so-called Panofsky equation [9]:

$$\Delta W_s = qU_g T \cos\varphi_s , \tag{2-1}$$

where q is the particle charge, φ_s the synchronous phase, T is the transit-time factor:

$$T = \frac{\sin \pi\alpha_g}{\pi\alpha_g} \cdot \left[\mathrm{I}_0\left(\frac{2\pi}{\beta_s \lambda} a \right) \right]^{-1} \equiv T_L(\alpha_g) \cdot T_R(a) \le 1 . \tag{2-2}$$

The gap factor α_g and the aperture radius a affect on the value of transit-time factor T , which determines the energy gain. The dependence of the longitudinal coefficient $T_L(\alpha_g)$ on the gap factor α at the injection energy is shown in Fig. 4,a. At the gap factor α_g =0.25, the value of the longitudinal coefficient, $T_L(\alpha_g)$ is equal to 0.90. With an energy growth the value of $T_L(\alpha_g)$ increases faster to the value $T_L(\alpha_g)$=1 for both our designs, since the "constant-voltage" design has the decreasing $\alpha_g(\beta_s)$-dependence, the "gradient-voltage" design has a constant $\alpha_g(\beta_s)$-dependence. The value α_g =0.25 has been chosen for both designs at injection energy.

The dependence of the radial coefficient $T_R(a)$ on the aperture radius a at the injection energy is shown in Fig. 4,b. The radial coefficient $T_R(a)$ decreases with the growth of the aperture radius a . To ensure a high acceleration rate, the value of $T_R(a)$ should be higher as possible. However, to ensure a high acceptance of the accelerator, the aperture radius a also should be high enough. At the aperture radius of 5 mm, the value of $T_R(a)$ has an appropriate value of 0.88. This value of the aperture radius has been chosen for both our designs, while the aperture radius is kept to be constant along the whole structures.

The dependence of the transit-time factor T on aperture radius at injection energy W_{inj} and at the double value of the injection energy $W = 2W_{inj}$ is shown in Fig 4,c. Because

$T_R(a)$ depends on the ratio a/β_s, the value of $T_R(a)$ increases to the value $T_R(a)$=1 with an energy growth. Note, there is a possibility to increase the aperture radius along the structure, still keeping a high value of the $T_R(a)$. Because the particle velocity increases by the factor 3 in our APhF linac, the aperture radius also can be increased by the same factor.

The potential and field distributions along the first accelerating cell at the injection energy are shown in Fig. 5. These distributions at the aperture radius $r = a$ are shown in Fig. 5,a. The distribution of potential along the line $r = a$ is similar to the linear dependence. The longitudinal component of the electrical field E_z is similar to the "square-wave" function. The radial component of the electrical field E_r is widely spread along the whole accelerating cell. It differs from an ideal pulse-type radial field for the "square-wave" approach.

The distributions along the cell axis $r = 0$ are shown in Fig. 5,b. On the cell axis the E_z-field has a bell shape and deeply penetrates inside drift tubes, reaching zero-values at the cell boundaries. The pattern of the E_z-field is strongly coupled with cell boundaries. The voltage distribution along the cell axis $r = 0$ is similar a sine-function, while the voltage on the gap axis, $U_g^{r=0}$ is smaller than voltage between drift-tubes, U_g. At the injection energy, the potential depression $U_g^{r=0}/U_g$ is equal to 0.94.

The results of calculations by POISSON code for the last cell of the "constant-voltage" design are shown in Fig. 6. The potential and field distributions at the aperture radius $r = a$ and on the cell axis $r = 0$ are shown in Fig. 6,b and Fig. 6,c, respectively.

One may conclude, that with an energy growth, distributions along the line $r = a$ become closer to distributions for an ideal "square-wave" approach. The radial component of the electrical field E_r is similar two pulses concentrated at the gap boundaries and does not penetrate inside drift-tubes. On the cell axis the E_z-field has is concentrated within the gap length and does not penetrate inside drift tubes. Similar graphs for the "gradient-voltage" design are shown in Fig. 7. The potential distributions along $r = a$ are also similar to the linear dependence.

Thus, the potential along the cell at $r = a$ can be approximated by the linear function for the whole length of both our APhF designs. This approach will be used at early stages of beam dynamics simulations. It allows us to calculate fields analytically and to avoid the calculations with POISSON code.

3. The APhF concept

The APhF belongs to the wide class of focusing methods by axially symmetrical RF fields, provided in sequences of drift-tubes with axially symmetrical cross-sections. The original APhF idea of beam focusing by a periodical alternating a synchronous phase in a sequence of the drift-tube gaps has been developed and modified since the early 50's by many authors. In the papers [3,5,6,11,12], there are comprehensive lists of references to the most known recipes of generating the drift-tube structures with required beam parameters.

Here, we will use focusing by RF fields of the drift-tube gaps in a spirit of a so-called asymmetrical alternative phase focusing (A-APhF), which has been proposed by V.V. Kushin in more than 30 years ago [11,12]. The A-APhF concept is well suited for our design. The A-APhF linac is able to provide a high-rate acceleration of short beam bunches, which can be delivered by the RFQ linac.

In this report, a sequence of drift-tube gaps is treated as periodical arrays of focusing and defocusing lenses for both longitudinal and radial motion. Besides of periodical sign-variable forces, these lens arrays provide non-zero average focusing forces. This means that distribution of periodical forces has an asymmetry. The asymmetry of the periodical forces allows to increase a portion of stable particles, because an operating point is shifted to a center of stability diagram. Following to the A-APhF concept, the average force for the longitudinal motion is defocusing, and the average force for the radial motion is focusing.

To analyze the A-APhF lens array, several approaches can be applied, e.g. a smooth approximation method, Matiew-Hill equations with one or several harmonics of a focusing force or a step-wise presentation of the focusing force. In this report, step-wise approach of the focusing force is used. With a concept of an equivalent accelerating wave [13], every RF gap is treated as a single thick lens with constant force.

Let's consider a general case of the phase sequence on the period of the phase excursion, $\varphi_s^{n_g}$ K $\varphi_s^{N_g}$. The number of drift-tube gaps in one focusing period is denoted as N_g. The focusing period of APhF linac L_f coincides with the period of phase excursions. The phase sequence can be written as the step-wise function $\varphi_s(\tau) = \overline{\varphi} + \widetilde{\varphi}(\tau)$. The variable part of the phase-alternating function $\widetilde{\varphi}(\tau)$ is constant within the every n_g-th accelerating period.

Following the notation adopted in papers [11-13], one can derive the motion equations for phase deviation ψ and radial position r using longitudinal coordinate Z_s as an independent variable. Let's introduce a dimensionless independent variable $d\tau = dZ_s / L_f$ and

dimensionless radial position $\rho = r/L_{\mathrm{f}}$. Small phase deviations ψ and a linear radial motion can be expressed by the following Matiew-Hill equations:

$$\begin{cases} d^2\psi/d\tau^2 + P_{\psi}(\tau)\cdot\psi = 0 \\ d^2\rho/d\tau^2 + P_{\rho}(\tau)\cdot\rho = 0 \end{cases}, \tag{3-1}$$

where the periodical step-wise functions $P_{\psi}(\tau) \equiv P_{\psi}(\tau+1)$ and $P_{\rho}(\tau) \equiv P_{\rho}(\tau+1)$ are given by

$$P_{\psi}(\tau) = 2B\cdot\sin[\overline{\varphi} + \widetilde{\varphi}(\tau)], \tag{3-2 }$$

$$P_{\rho}(\tau) = -B\cdot\sin[\overline{\varphi} + \widetilde{\varphi}(\tau) + \psi], \tag{3-2}$$

with the focusing strength B given by

$$B = \frac{\pi q E_{\mathrm{m}}}{m_o c^2}\frac{\lambda}{\beta_{\mathrm{s}}}\left(\frac{L_{\mathrm{f}}}{\beta_{\mathrm{s}}\lambda}\right)^2\left(1-\beta_{\mathrm{s}}^2\right)^{3/2}. \tag{3-4}$$

In the equation (3-4), E_{m} denotes the amplitude of an equivalent accelerating wave, which can be expressed as a product of an average electrical field in the accelerating cell and the transit-time factor, i.e., $E_{\mathrm{m}} = E_0 T$.

The above motion equations (3-1) are the Matiew-Hill equations with periodical step-wise functions. They have been solved using a matrix technique, which is well known in the linear accelerator theory [14]. To analyze solutions of these equations it is convenient to use the so-called Smith-Gluckstern stability diagrams. The RMS and average values of functions $P_{\psi}(\tau)$ and $P_{\rho}(\tau)$ have been used to build stability diagrams. The stability diagrams can be built for the integer even numbers of $N_{\mathrm{g}} \geq 2$.

In the matrix formalism, the matrices of the focusing period are obtained by multiplying in proper order the corresponding matrices of every drift-tube gap. The product matrix of the symmetrical focusing period is of the form [13]

$$M_{\mathrm{f}} = \begin{bmatrix} \cos\mu & \dfrac{\sin\mu}{\nu} \\ -\nu\sin\mu & \cos\mu \end{bmatrix}. \tag{3-5}$$

In APhF linacs for heavy ions the number of RF gaps in focusing period $N_{\mathrm{g}} >> 2$ [3]. In our design, the number N_{g} is more than 10. The matrices of the focusing period have been calculated numerically. The stability diagrams have built using procedures of the mathematical package MAPLE V [15].

Figure 8 shows dependence of synchronous phase within a focusing period $\varphi_{\mathrm{s}}(\tau)$, the necktie stability diagram for longitudinal and transverse motion, and a radial stability diagram with

non-synchronous particles at the injection energy. Figure 8,b and Figure 8,c are built on the radial plane $\left\{\overline{P}_\rho; P_\rho^{\mathrm{RMS}}\right\}$. The circle and cross marks are used to show positions of position of synchronous and non-synchronous particles, respectively. For the strong focusing it is quit usual to ask that the representative point should stay inside the stable region for all captured ions at all times. In Fig. 8,b, the operating point is near the intersection of the curves $\cos\mu_{\mathrm{L}} = 0$ and $\cos\mu_{\mathrm{R}} = 0$.

According to the equations 3-4, with increasing the particle velocity, the focusing strength B is decreased. For the "constant-voltage" design with $E_{\mathrm{m}} \propto 1/\beta_{\mathrm{s}}$, the focusing strength B decreases faster as $B \propto N_{\mathrm{g}}^2(\beta_{\mathrm{s}})/\beta_{\mathrm{s}}^2$, and for the "gradient-voltage" design with a constant E_{m}, the focusing strength B decreases slowly as $B \propto N_{\mathrm{g}}^2(\beta_{\mathrm{s}})/\beta_{\mathrm{s}}$.

To keep the focusing strength and a position of operating point in the center of stability diagram, it is necessary to increase N_{g} along the whole structure. The number N_{g} should be changed slowly in the case of the "gradient-voltage" design ($N_{\mathrm{g}} \propto \sqrt{\beta_{\mathrm{s}}}$) in a comparison with the "constant-voltage" design ($N_{\mathrm{g}}(\beta_{\mathrm{s}}) \propto \beta_{\mathrm{s}}$). Figure 9 shows the dependence of N_{g} on the particle energy along whole APhF structure for both our designs.

In paper [6], it is recognized, that when the number N_{g} changes abruptly, there are a serious mismatch of either or both the transverse and longitudinal motion, which lead to a growth of the beam emittance. The authors are pointed out, that it is necessary to devise some method to change N_{g} adiabatically, or construct some alternate method of phase space matching, to eliminate the emittance growth.

In the reference [12], several tables with parameters of A-APhF linacs are presented. Those APhF designs use non-integer values of N_{g}. Although it is not explicitly written in the paper text, one may assume that number N_{g} change continuously in those A-APhF designs. We have decided to use the number N_{g} as a floating-number function of the particle velocity in mathematical procedures of generating APhF accelerating cells, i.e., N_{g} α $N_{\mathrm{g}}(\beta_{\mathrm{s}})$.

4. Generation of APhF drift-tube structure

Table 2 shows main steps during process of generation and analysis of APhF linac. These steps include the choice of the operation point on the stability diagram, the application of some theoretical approach to the RF field in the accelerating cells, generating drift tube sizes, and beam tracing. For every step, several options are available. The double line in Table 2 shows our choice from possible options.

The parameters of our APhF designs have been essentially determined by a requirement to keep a position of operating point in the center of stability diagram and by an applying restrictions on the RF field parameters described in Section 2. The procedure of the stability analysis with a help of Smith-Gluckstern stability diagrams for Matiew-Hill equation has been outlined in the previous section. On this step, the concept of equivalent accelerating wave has been used as a theoretical approach to the RF field in the drift-tube gaps.

For both our designs the stability diagrams have been built throughout whole linacs at even numbers N_g. The phase advances of the longitudinal and transverse oscillations on the length of the focusing period for both our designs are shown in Fig. 10. During arrangement of operating points on stability diagrams, the linac parameters have been calculated at even numbers N_g. Then, linac parameters have been interpolated as a function of the particle velocity. Using these dependences, drift-tube generation procedure has been performed.

Several analytical and numerical procedures for a generation of geometric dimensions of drift-tube linacs are known, e.g. Ref. [16,17]. Basically, these algorithms have been developed for conventional Alvarez-type linacs, where drift-tube lengths monotonically increase along the linac and the cell length is equal to $h\beta_s\lambda$, where h is the harmonic number. For example, the Swenson's algorithm [16] for Alvarez cells uses combination of analytical formulae and numerically calculated moments of the field distribution along the accelerating cells (also known as transit-time coefficients). Due to large alternations of the synchronous phase in APhF linac, the length of accelerating cells excurse periodically around $h\beta_s\lambda$-value. As result, some Swenson's constrains are not fulfilled well in the case of APhF.

To avoid systematic errors in calculations of the drift-tube lengths coming from an analytical approaches, we have realized a numerical procedure based on a direct numerical solution of the motion equations. First, preliminary values of the cell lengths have been calculated using a simple numerical iterative process described in Ref. [17]. It is based on Panofsky's eq. (2-1) and performs iterations to the average value of the particle velocity

within every accelerating cell. Second, the gap center is shifted to ensure the programmed value of the synchronous phase. Finally, the drift tube dimensions have been additionally corrected with a numerical integration of the motion equations, which have been solved by the Runge-Kutta method. The electrical fields in the gaps have been calculated using a linear interpolation of the potential between drift-tubes at the radius $r = a$.

Electrical fields in the acceleration gap have been be derived in the electrostatic approach, which is usually used for low-energy linacs [17]. Electrical field is calculated as a gradient of the potential, $\vec{E} = -\nabla U$. The potential inside the cylindrical volume is presented as Fourier-Bessel series with the period $L = \beta_s \lambda$:

$$U(r,z) = U_0 + \sum_j \left\{ I_0\left(\frac{2\pi j}{L} r\right)\left[A_j \cos\left(\frac{2\pi j}{L} z\right) + B_j \sin\left(\frac{2\pi j}{L} z\right)\right] \Big/ I_0\left(\frac{2\pi j}{L} a\right)\right\} \quad (4\text{-}1)$$

Using a given potential distribution on the cylindrical surface $r = a$, the coefficients of the series are defined using the numerical harmonical analysis. The potential values at $r = a$ can be calculated using some numerical code, e.g., POISSON code. Examples of the field calculations with POISSON code have been presented in Section 2. For a fast beam dynamics simulations we used a linear approach to the potential distribution on the cylindrical surface $r = a$, which is widely used in linac codes [18].

To avoid time-consuming numerical calculations of Fourier-Bessel series, we used a paraxial approximation to the potential. In paraxial approximation, the axially symmetrical potential is expressed by the series

$$U(r,z) \cong U(0,z) - \frac{r^2}{2^2} U''(0,z) + \mathrm{K} + \frac{(-1)^n}{(n!)^n}\left(\frac{r}{2}\right)^{2n} U^{(2n)}(0,z), \quad (4\text{-}2)$$

where the function $U(0,z)$ is the potential distribution on the axis $r = 0$. This function is calculated using a cubic-spline interpolation for the values of $U(0,z_n)$, which has been calculated from the above Fourier-Bessel series for potential.

The synchronous phase and the reference particle energy vs cell number for the "constant-voltage" design and for the "gradient-voltage" design are shown in Fig. 11. The "gradient-voltage" design with 48 RF gaps and total length 2.137 m is almost twice shorter then the "constant-voltage" design with 88 RF gaps and total length 4.213 m. Parameters of accelerating cells for both designs are presented in Table 3 and Table 4.

5. Beam dynamics simulations

In order to obtain the characteristics of an accelerated beam, numerical beam dynamics simulations have been performed. We have used the beam dynamic code DYN1 written by Kapin. This code has been previously tested for RFQ structures and showed a good agreement with PARMTEQ code. This code simulates the motion of particles without space-charge effects between particles of the beam. The motion equations are solved by the numerical integration using the Runge-Kutta method. The external fields are formulated in a quasi-static approximation:

$$\vec{\mathbf{E}} = \vec{\mathbf{E}}^{=} + \vec{\mathbf{E}}^{\sim}\cos(\omega t + \Psi_E); \quad \vec{\mathbf{B}} = \vec{\mathbf{B}}^{=} + \vec{\mathbf{B}}^{\sim}\cos(\omega t + \Psi_B), \tag{5-1}$$

where the electromagnetic fields $\vec{\mathbf{E}}$ and $\vec{\mathbf{B}}$ are the sums of static ($\vec{\mathbf{E}}^{=}, \vec{\mathbf{B}}^{=}$) and time-variable components $\vec{\mathbf{E}}^{\sim}, \vec{\mathbf{B}}^{\sim}$ with an angular frequency ω.

The following notation of the motion equations in RF electrical fields is used by DYN1 code:

$$\begin{cases} \dfrac{d\varphi}{dz} = \dfrac{2\pi}{\beta_z \lambda} \\ \dfrac{d\beta_z}{dz} = \dfrac{Z_{\mathrm{i}} q_{\mathrm{p}}}{A_{\mathrm{i}} m_{\mathrm{amu}} c^2} \dfrac{1}{\beta_z \gamma_z^3} E_z \\ \dfrac{d^2x}{dz^2} = \dfrac{Z_{\mathrm{i}} q_{\mathrm{p}}}{A_{\mathrm{i}} m_{\mathrm{amu}} \gamma_z c^2} \dfrac{1}{\beta_z^2} E_x - \left[\dfrac{1}{\beta_z} + \beta_z \gamma_z^2\right] \dfrac{d\beta_z}{dz} \dfrac{dx}{dz}, \\ \dfrac{d^2y}{dz^2} = \dfrac{Z_{\mathrm{i}} q_{\mathrm{p}}}{A_{\mathrm{i}} m_{\mathrm{amu}} \gamma_z c^2} \dfrac{1}{\beta_z^2} E_y - \left[\dfrac{1}{\beta_z} + \beta_z \gamma_z^2\right] \dfrac{d\beta_z}{dz} \dfrac{dy}{dz} \end{cases} \tag{5-2}$$

where $\varphi = \omega t$ is the particle phase; $\beta_z = v_z / c$ is the relative particle velocity; c is the velocity of light; Z_{i} and A_{i} are the charge state and atomic number of ion, respectively; ; q_{p} is the elementary charge; m_{amu} is the mass of nucleon; $\{E_x, E_y, E_z\}$ are the components of the RF electric field; $\gamma_z = \left(1 - \beta_z^2\right)^{-1/2}$ is the Lorentz factor. The beam dynamics in APhF has been calculated under the non-relativistic approximation, $\gamma_z \approx 1$.

The results of beam dynamics simulations for the “constant-voltage” design are presented in Fig.12-16. The longitudinal acceptance of particles moving along the axis and the energy spectrum of passed particles are shown in Fig. 12. The phase capture is about 30 degrees. This is a typical value for A-APhF linacs [11,12]. For example, and GSI’s design [3] has a similar longitudinal capture. The almost all captured particles reach the given output energy $W = 4$ MeV/u. Energy spectrum has a sharp peak at this energy.

Fig. 13 shows transverse acceptances of the "constant-voltage" design.

Due to the strong coupling of the longitudinal and transverse motions, the transverse acceptance of APhF linac depends of the longitudinal parameters of the beam. Several transverse acceptances for particular longitudinal parameters of the beam are shown in Fig. 13. The shapes of particular transverse acceptances are very different.

Usually, the so-called effective acceptance is defined. It is a common area of particular acceptances. The transverse effective acceptance is equal to $15\ \pi\text{mm}\times\text{mrad}$ (GSI case [3] $13\ \pi\text{mm}\times\text{mrad}$). To ensure the radial stability of the particles injected within the longitudinal acceptance, the radial emittance of the injected beam should be less or equal to the effective radial acceptance. Thus, emittance of beam injected into the APhF linac from the RFQ is determined by acceptances shown in Fig. 12 and Fig. 13.

The dependence of the beam transmission on the relative voltage amplitude in IH-APhF tank for the "constant-voltage" design is shown Fig. 14. The emittances of the injected beam determined above are shown in Figure 15. The results of Fig. 14 show that the beam transmission of the injected beam can reach 85 %. Also, Fig. 14 demonstrates that the APhF structure is very sensitive to a small voltage deviation of order 1%.

Figure 16 shows the transverse and longitudinal emittances of the passed particles for the "constant-voltage" design. The transverse emittance of the output is about $8\ \pi\text{mm}\times\text{mrad}$. The phase portrait of the beam in the longitudinal phase-space has a long tail smearing over about 50 degrees. The energy spread is about $\Delta W/W \approx \pm 0.8\%$. The requirement for the energy spread of output beam is $\Delta W/W \le \pm 0.4\%$. In order to reduce the energy spread of output beam, a phase-space portrait of beam should be "rotated". It can be done by scaling the amplitude of the phase law (Fig.11,a) with the coefficient 0.95. A new structure consisting of 86 cells provides a beam with a smaller energy spread (see Fig. 16) $\Delta W/W \approx \pm 0.4\%$, which is close to the above-required value.

Some results of beam dynamics simulations for the "gradient-voltage" design are presented in Fig. 17. In comparison with the "constant-voltage" design, the longitudinal acceptance is a little bit larger, the longitudinal emittance of output beam is smaller, and the beam transmission is higher (92%). In view point of beam dynamics a short "gradient-voltage" design is more attractive than the "gradient-voltage" design.

6. Effects of Random Errors

The APhF is based on the principle of the strong focusing for both the longitudinal and the transverse motion. It is know that a serious problem to the strong focusing is an extreme sensitivity to random errors in the positions and strength of the lens elements [14]. In the case of the APhF, there is a strong dependence of a beam quality on small drift-tube misalignments along structure and on fluctuations of the gap voltages about programmed values [3,7].

Analytical approaches for the calculation of induced oscillations due to random errors in strong focusing linacs have been developed in Ref. [13,14,17]. According to these approaches, the mean-square induced amplitude δA_{rms} determines the level of permissible errors. δA_{rms} is the sum of the mean-square contributions of Ξ individual lens elements δa_{rms}:

$$\delta A_{\mathrm{rms}} = \Xi \cdot \delta a_{\mathrm{rms}} . \tag{6-1}$$

Thus, the structure with a smaller number of the individual lenses is less sensitive to random errors. This means that the "constant-voltage" design with $\Xi = 88$ may provide a larger amplitude of the random oscillations than the "gradient-voltage" design ($\Xi = 48$).

The amplitude δa_{rms} has a factor $1/\nu$, i.e. inversely proportional to the amplitude coefficient ν determined by the matrix of the focusing period (3-5). The quantity ν is generally small, approaching to zero value at the boundaries of the stability diagram. This means that effects of random errors become more serious when the position of an operating point on the stability diagram is near the boundaries. To reduce effects of random errors the operating point should stay within a center of the stable area.

The analytical formulae for effects of random errors in an accelerator with focusing by an axial-symmetrical accelerating field have been derived by V.K. Baev and are presented in Ref. [7]. The formulae can be used for APhF linac, which is a kind of the focusing by an axial-symmetrical accelerating field.

The radial induced amplitude $\delta a^{r}_{\mathrm{rms}}$ contributed by random errors in drift-tube positions δ_r and amplitudes of the electrical fields in gaps δ_E can be evaluated as [7]:

$$\delta a^{r}_{\mathrm{rms}} = \frac{L_{\mathrm{f}}^2 \Omega^2}{\lambda^2 \nu_r N_g} \sqrt{\frac{\delta_r^2}{6} + \frac{R_{\max}^2}{24} \delta_E^2} , \tag{6-2}$$

$$\text{with } \Omega^2 = \pi A_{\mathrm{m}} \sin\varphi_{\mathrm{s}} / \beta_{\mathrm{s}}^3 \text{ and } A_{\mathrm{m}} = qE_{\mathrm{m}}\lambda / \mathrm{m}_0 c^2 ,$$

where $L_{\mathrm{f}} = N_g h \beta_{\mathrm{s}} \lambda$ is the length of the focusing period, ν_r is an amplitude coefficient for radial motion. Let's evaluate the level of permissible errors for the "constant-voltage" design

($\Xi = 88$) with parameters given at the injection energy, i.e., $N_{\mathrm{g}} = 10$, $R_{\max}$ =5 mm, $\beta_{\mathrm{s}} = 0.03$, $\varphi_{\mathrm{s}} = \pi/2$, $E_{\mathrm{m}} = 6$ MeV/m, $\nu_r = 0.9$.

For the position displacements δ_r =100 μ m, the mean-square induced amplitude δA_{rms} is about 0.5mm at an amplitude fluctuations δ_E =5%, and δA_{rms} is about 1 mm at δ_E =10%. At displacements δ_r =500 μ m and amplitude fluctuations δ_E =10%, the mean-square induced amplitude δA_{rms} is large (about 2mm) and may lead to the considerable beam loss.

One may conclude, that the level of permissible errors for the drift-tube displacements is up to several 100 μ m and for the fluctuations of the gap voltages is about 5-10 %. A careful technology for mechanical assembling and RF measuring can ensure these levels of precision. The more detailed study of the effects of random error requires additional beam dynamics simulations and is not considered in this report.

7. Feasibility of a gradient-type voltage in IH-cavity

The "gradient-voltage" design has some advantages. However, the realization a gradient type of the voltage distribution in IH-cavity might be difficult. It requires special tuning elements and may affect on value of the shunt impedance. The detailed studies of such tuning procedure and its influence on the shunt impedance can be found in papers [19,20].

Several IH-type linacs use a gradient-type voltage distribution [8,21]. The very close example for our design is the GSI 7 MeV/u 217 MHz IH-type KONUS linac [8], which uses a gradient type of the voltage distribution. In this GSI linac, the gap voltage is ramped from 200 kV to 480 kV along the 3.8 m long structure.

The preliminary calculations by Microwave Studio code [22] has been performed for the cavity with the total length 2 m. Drift tube structure has uniform parameters: the gap length is 1 cm and the drift-tube length 4 cm. Figure 18 shows the internal layout of resonator and Fig. 19 shows the voltage distributions along the cavity. The voltage amplitude increases about 3 times along the cavity and differs from an ideal dependence. The beam dynamics calculations for an realistic voltage distribution will be performed in the near future.

References

[1] Y. Hirao et. al., "Heavy Ion Synchrotron for Medical Use" Nucl. Instrum. & Methods in Phys. Res., A538, 541c (1992).

[2] S. Yamada, NIRS, "The Progress of HIMAC and Particle Therapy Facilities in Japan", Proc. Second Asian Particle Accelerator Conference (APAC'01), pp.829-833.

[3] S. Minaev, U. Ratzinger, B. Schlitt , "APF or KONUS drift tube structures for medical synchrotron injectors – a comparison", Proceedings of the 1999 Particle Accelerator Conference, New York, 1999, pp.3555-3557.

[4] S. Yamada et al, "Injector System of HIMAC", Proceedings of the 1990 Linear Accelerator Conference, LANL, 1990, pp. 593-595.

[5] H. Okamoto, "Beam Dynamics in Alternating Phase Focusing Linac", Nucl. Instr. & Meth. in Phys. Res., A 284, 1989, pp. 233-247.

[6] W.H. Cheng, R.L. Gluckstern, S. Nath, T.P. Wangler, "Alternating Phase Focusing Including Space Charge", Proc. of the 1992 Linear Accelerator Conference, Ottawa, Canada, 1990, pp. 193-195.

[7] V.K. Baev, "Effects of errors on the Particles Dynamics in Accelerator with Focusing by an Axial-Symmetrical Accelerating Field", In collected papers of Moscow Engineering Physics Institute: "Accelerator-Based Radiative-Acceleration Complexes", Moscow, Energoatomizdat, 1983, pp. 39-42 (in Russian).

[8] B. Schlitt et al, "Design of the 7 MeV/u, 217 MHz Injector Linac for the Proposed Ion beam Facility for Cancer Therapy at the Clinic in Heidelberg", Proc. of the XX International Linac Conference, Monterey, 2000, pp. 226-228.

[9] T.P. Wangler, "Principles of RF Linear Accelerators", 1998, J. Wiley & Sons, Inc.

[10] J.H. Billen and L.M. Young, "Poisson/Superfish" LA-UR-96-1834, 2002.

[11] V.V. Kushin, "Ion Acceleration in APF systems", Proceedings of the 1994 Int. Linac Conf., Tsukuba, Japan, pp. 957-961.

[12] V.V. Kushin, "Accelerator with Alternating Phase Focusing", Ch. 7 in book: "Linear ion accelerators", ed. By B.P.Murin, 1978 (in Russian), pp.173-208.

[13] A.D. Vlasov, "Theory of linear accelerators", Moscow, 1965 by Atomizdat (in Russian, there is an English translation published in Tel-Aviv).

[14] L. Smith and R.L. Gluckstern, "Focusing in Linear Ion Accelerators", The Review of Scientific Instrum., Vol. 26, No. 2, 1955, pp. 220-228.

[15] M.B. Monagan et al, MAPLE V – Programming Guide, 1998 by Waterloo Maple Inc.

[16] D. Swenson, “Generation of Geometrical Dimensions for Drift Tube Linacs”,
report MP-3/DAS-1, 1967

[17] I.M. Kapchinskiy, “Theory of Resonance Linear Accelerators”, Harwood Academic Publishers, Amsterdam, 1985.

[18] Y.K. Batygin, “Particle-in Cell Code BEAMPASS for Beam Dynamics Simulations with Space Charge”, report RIKEN-AF-AC-17, 2000 by Inst. Phys. & Chem. Res. (RIKEN).

[19] S. Yamada et al, “IH Linac Development at INS”, report INS-NUMA-57, 1985 by Institute for Nuclear Study, Tokyo Univ.

[20] B. Krietenstein et al, “Numerical Simulation if IH Accelerators with MAFIA and RF model measurements”, Proc. of VIII International Linear Accelerator Conf., Geneva, 1996, pp. 243-245.

[21] K. Isokawa et al, “Development of High Gradient IH Linac”, Nucl. Instr. & Meth. in Phys. Res., A 415, 1998, pp. 287-290.

[22] “CST MICROWAVE STUDIO”, WWW: http://www.cst-world.com.

Table 1. The injector linac specification

Total length of “RFQ+APhF” tanks	< 5 m
Ion species	$^{12}C^{+4}$
RFQ linac	
Tank length	< 2 m
Frequency (wavelength)	200 MHz (1.49 m)
Input/Output energy	8 / 400-500 keV/u
Max. surface field	236 kV/cm(1.6 Kilpatrick)
Peak rf power	< 100 kW
APhF linac	
Tank length	2-3 m
Frequency	200 MHz
Input energy	400-500 keV/u
Output energy	4 MeV/u
Max. surface field	236 kV/cm (1.6 Kilpatrick)
Internal corner radius of DT	>2 mm

Table 2. Design steps for APhF linac

<table>
<tr><th>Operating point analysis – Stability diagram</th><th colspan="2">Theoretical Approach to the RF field in cells</th><th>Generating drift tube structure</th><th>Beam tracing</th><th colspan="2">RF Voltage in RF resonator</th></tr>
<tr><td>Kushin's (1970) approximation with $\varphi_s = \varphi_0 \pm \varphi_1$</td><td colspan="2">Concept of an equivalent accelerating wave
(Average field and Transit-time Factor)</td><td>Swenson; Kapchinskii
(Panofsky equation: $\Delta W_s = qE_0TL_{cell}\cos\varphi_s$)</td><td>Semi-analytical particle tracing – map's multipliation</td><td rowspan="5">RF tests & measure-ments in model cavity</td><td rowspan="5">RF code with MWS;MAFIA etc.</td></tr>
<tr><td>Smith-Gluckstern diagram for step-wise Hill-Matiew equation (heavy ions $\varphi_s \approx \varphi(z)$ - $N_g >> 2$)</td><td colspan="2">Square-wave approximation
(constant field in the gap)</td><td>Swenson; Murin-text book: analytical formulae</td><td>Semi-analytical particle tracing – map's multipliation (MRTI; MEPhI)</td></tr>
<tr><td rowspan="3">Smooth-approximation of focusing force:
Matiew equation
(Okamoto, 1989)</td><td rowspan="2">Linear filed distribution on cell aperture r=a</td><td>Linear paraxial approximation with splines</td><td>Correcting synchronous phase in cells created by analytical procedure with accelerating wave</td><td>Numerical integration (Runge-Kutta method)</td></tr>
<tr><td>Full Fourier-Bessel Series</td></tr>
<tr><td>The field distribution on cell aperture r=a by numerical code (POISSON)</td><td>Linear paraxial approximation
Full Fourier-Bessel Series</td></tr>
<tr><td colspan="3">More full RF fields in structure
(3D; E-M fields with a space-charge effects of beam)</td></tr>
</table>

Table 3. Cell parameters for the “constant-voltage” design

Cell No	U_g, V	L_{cell}, m	l_{entr}, m	l_g, m	l_{exit}, m	a, m	ϕ_s, deg
1	173000	0.0224	0.0034	0.011	0.008	0.005	-60.0
2	173000	0.0276	0.0075	0.011	0.009	0.005	-28.0
3	173000	0.0294	0.0085	0.011	0.010	0.005	9.0
4	173000	0.0301	0.0096	0.011	0.009	0.005	49.8
5	173000	0.0294	0.0094	0.011	0.009	0.005	78.4
6	173000	0.0256	0.0090	0.011	0.006	0.005	99.6
7	173000	0.0221	0.0056	0.011	0.005	0.005	73.7
8	173000	0.0214	0.0055	0.011	0.005	0.005	45.2
9	173000	0.0220	0.0048	0.011	0.006	0.005	3.8
10	173000	0.0242	0.0058	0.011	0.007	0.005	-27.4
11	173000	0.0260	0.0069	0.011	0.008	0.005	-49.0
12	173000	0.0298	0.0077	0.011	0.011	0.005	-65.4
13	173000	0.0334	0.0107	0.011	0.012	0.005	-47.6
14	173000	0.0347	0.0111	0.011	0.013	0.005	-28.5
15	173000	0.0375	0.0120	0.011	0.014	0.005	-5.2
16	173000	0.0381	0.0140	0.011	0.013	0.005	33.5
17	173000	0.0367	0.0128	0.011	0.013	0.005	52.7
18	173000	0.0367	0.0128	0.011	0.013	0.005	67.7
19	173000	0.0349	0.0128	0.011	0.011	0.005	80.6
20	173000	0.0325	0.0110	0.011	0.010	0.005	73.5
21	173000	0.0320	0.0104	0.011	0.011	0.005	59.3
22	173000	0.0320	0.0105	0.011	0.010	0.005	43.6
23	173000	0.0306	0.0103	0.011	0.009	0.005	23.5
24	173000	0.0319	0.0090	0.011	0.012	0.005	-12.2
25	173000	0.0352	0.0114	0.011	0.013	0.005	-27.1
26	173000	0.0368	0.0124	0.011	0.014	0.005	-36.3
27	173000	0.0383	0.0130	0.011	0.014	0.005	-42.3
28	173000	0.0403	0.0138	0.011	0.015	0.005	-43.6
29	173000	0.0418	0.0150	0.011	0.016	0.005	-37.0
30	173000	0.0426	0.0153	0.011	0.016	0.005	-30.5
31	173000	0.0436	0.0157	0.011	0.017	0.005	-23.3
32	173000	0.0484	0.0164	0.011	0.021	0.005	-13.8
33	173000	0.0495	0.0206	0.011	0.018	0.005	27.5
34	173000	0.0462	0.0176	0.011	0.018	0.005	40.3
35	173000	0.0458	0.0173	0.011	0.018	0.005	47.3
36	173000	0.0459	0.0173	0.011	0.018	0.005	52.4
37	173000	0.0461	0.0174	0.011	0.018	0.005	56.5
38	173000	0.0457	0.0175	0.011	0.017	0.005	59.8
39	173000	0.0452	0.0170	0.011	0.017	0.005	57.0
40	173000	0.0454	0.0171	0.011	0.017	0.005	53.5
41	173000	0.0457	0.0172	0.011	0.018	0.005	49.5
42	173000	0.0457	0.0173	0.011	0.018	0.005	44.6
43	173000	0.0405	0.0172	0.011	0.012	0.005	37.4
44	173000	0.0406	0.0120	0.011	0.018	0.005	-10.6
45	173000	0.0469	0.0171	0.011	0.019	0.005	-21.8
46	173000	0.0486	0.0183	0.011	0.019	0.005	-26.8
47	173000	0.0495	0.0188	0.011	0.020	0.005	-30.0
48	173000	0.0503	0.0192	0.011	0.020	0.005	-32.1
49	173000	0.0511	0.0196	0.011	0.021	0.005	-33.7
50	173000	0.0521	0.0199	0.011	0.021	0.005	-34.5
51	173000	0.0530	0.0206	0.011	0.022	0.005	-32.5
52	173000	0.0536	0.0209	0.011	0.022	0.005	-30.6
53	173000	0.0542	0.0211	0.011	0.022	0.005	-28.6
54	173000	0.0549	0.0215	0.011	0.022	0.005	-26.3
55	173000	0.0559	0.0218	0.011	0.023	0.005	-23.4
56	173000	0.0645	0.0225	0.011	0.031	0.005	-18.3

Cell No	U_g, V	L_{cell}, m	l_{entr}, m	l_g, m	l_{exit}, m	a, m	ϕ_s, deg
57	173000	0.0650	0.0306	0.011	0.023	0.005	37.2
58	173000	0.0573	0.0231	0.011	0.023	0.005	42.0
59	173000	0.0572	0.0229	0.011	0.023	0.005	44.1
60	173000	0.0574	0.0230	0.011	0.023	0.005	45.4
61	173000	0.0577	0.0231	0.011	0.024	0.005	46.1
62	173000	0.0580	0.0233	0.011	0.024	0.005	46.5
63	173000	0.0583	0.0235	0.011	0.024	0.005	46.8
64	173000	0.0584	0.0236	0.011	0.024	0.005	46.4
65	173000	0.0587	0.0236	0.011	0.024	0.005	45.2
66	173000	0.0591	0.0239	0.011	0.024	0.005	44.1
67	173000	0.0595	0.0240	0.011	0.024	0.005	42.9
68	173000	0.0598	0.0242	0.011	0.024	0.005	41.6
69	173000	0.0603	0.0245	0.011	0.025	0.005	40.0
70	173000	0.0598	0.0245	0.011	0.024	0.005	37.9
71	173000	0.0517	0.0244	0.011	0.016	0.005	33.0
72	173000	0.0526	0.0163	0.011	0.025	0.005	-20.4
73	173000	0.0617	0.0251	0.011	0.026	0.005	-23.3
74	173000	0.0627	0.0257	0.011	0.026	0.005	-24.9
75	173000	0.0633	0.0260	0.011	0.026	0.005	-26.1
76	173000	0.0637	0.0262	0.011	0.026	0.005	-26.9
77	173000	0.0643	0.0266	0.011	0.027	0.005	-27.7
78	173000	0.0648	0.0268	0.011	0.027	0.005	-28.3
79	173000	0.0653	0.0269	0.011	0.027	0.005	-28.8
80	173000	0.0660	0.0272	0.011	0.028	0.005	-28.8
81	173000	0.0665	0.0275	0.011	0.028	0.005	-28.3
82	173000	0.0671	0.0277	0.011	0.029	0.005	-27.7
83	173000	0.0673	0.0277	0.011	0.029	0.005	-27.0
84	173000	0.0681	0.0281	0.011	0.029	0.005	-26.2
85	173000	0.0686	0.0282	0.011	0.030	0.005	-25.1
86	173000	0.0692	0.0283	0.011	0.030	0.005	-23.7
87	173000	0.0703	0.0286	0.011	0.031	0.005	-21.6
88	173000	0.0697	0.0296	0.011	0.029	0.005	-16.1

The total length is 4.213 m

Table 4. Cell parameters for the “gradient-voltage” design

Cell No	U_g, V	L_{cell}, m	l_{entr}, m	l_g, m	l_{exit}, m	a, m	ϕ_s, deg
1	175300	0.0226	0.0035	0.0111	0.0080	0.005	-59.8
2	181800	0.0277	0.0072	0.0116	0.0089	0.005	-27.9
3	190800	0.0298	0.0081	0.0121	0.0096	0.005	10.7
4	198600	0.0304	0.0090	0.0126	0.0087	0.005	53.0
5	202300	0.0290	0.0086	0.0128	0.0076	0.005	81.9
6	202600	0.0251	0.0075	0.0129	0.0047	0.005	94.5
7	204100	0.0221	0.0046	0.0130	0.0045	0.005	67.5
8	210000	0.0213	0.0043	0.0133	0.0037	0.005	36.2
9	218900	0.0224	0.0031	0.0139	0.0054	0.005	-10.0
10	228000	0.0252	0.0046	0.0145	0.0061	0.005	-38.2
11	234600	0.0289	0.0054	0.0149	0.0086	0.005	-59.0
12	240500	0.0332	0.0078	0.0153	0.0101	0.005	-52.0
13	248100	0.0358	0.0092	0.0158	0.0109	0.005	-31.2
14	257700	0.0394	0.0098	0.0164	0.0132	0.005	-6.5
15	267000	0.0402	0.0123	0.0170	0.0109	0.005	38.8
16	274000	0.0382	0.0104	0.0174	0.0104	0.005	57.4
17	278700	0.0371	0.0101	0.0177	0.0093	0.005	70.0
18	282300	0.0350	0.0090	0.0179	0.0081	0.005	70.2
19	287000	0.0340	0.0078	0.0182	0.0080	0.005	57.0
20	293900	0.0315	0.0076	0.0187	0.0053	0.005	41.3
21	303200	0.0321	0.0046	0.0193	0.0082	0.005	-2.7
22	313400	0.0368	0.0072	0.0199	0.0097	0.005	-23.7
23	322900	0.0396	0.0087	0.0205	0.0104	0.005	-33.1
24	331500	0.0421	0.0093	0.0211	0.0117	0.005	-38.8
25	340100	0.0447	0.0106	0.0216	0.0125	0.005	-35.9
26	349200	0.0464	0.0113	0.0222	0.0130	0.005	-29.4
27	359000	0.0524	0.0118	0.0228	0.0179	0.005	-21.5
28	369000	0.0553	0.0167	0.0234	0.0152	0.005	21.5
29	378200	0.0519	0.0143	0.0240	0.0136	0.005	41.5
30	385900	0.0508	0.0129	0.0245	0.0134	0.005	47.7
31	393000	0.0510	0.0128	0.0249	0.0133	0.005	51.4
32	399600	0.0509	0.0127	0.0254	0.0128	0.005	52.6
33	406500	0.0510	0.0123	0.0258	0.0130	0.005	49.3
34	413900	0.0516	0.0124	0.0263	0.0130	0.005	45.4
35	421900	0.0447	0.0124	0.0268	0.0056	0.005	39.9
36	431300	0.0455	0.0048	0.0274	0.0133	0.005	-16.6
37	441500	0.0547	0.0122	0.0280	0.0145	0.005	-24.8
38	451300	0.0570	0.0134	0.0286	0.0150	0.005	-27.5
39	460900	0.0586	0.0139	0.0293	0.0155	0.005	-28.7
40	470500	0.0603	0.0143	0.0299	0.0161	0.005	-29.1
41	480100	0.0618	0.0149	0.0305	0.0165	0.005	-27.6
42	489900	0.0631	0.0152	0.0311	0.0168	0.005	-26.1
43	499800	0.0646	0.0155	0.0317	0.0173	0.005	-24.4
44	509800	0.0759	0.0160	0.0324	0.0276	0.005	-22.0
45	519400	0.0774	0.0263	0.0330	0.0181	0.005	34.8
46	528200	0.0687	0.0172	0.0335	0.0180	0.005	38.9
47	536600	0.0693	0.0170	0.0341	0.0182	0.005	40.8
48	544800	0.0697	0.0173	0.0346	0.0179	0.005	42.5

The total length is 2.137 m

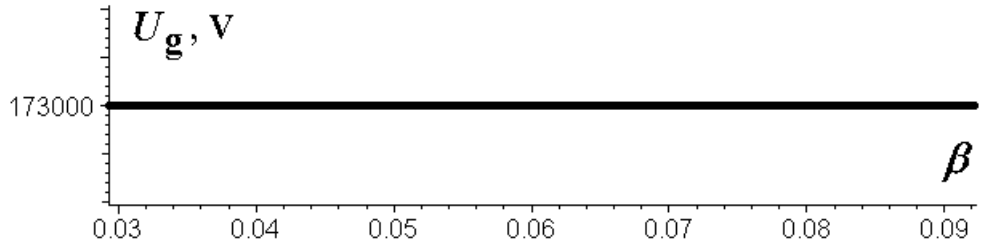

a)

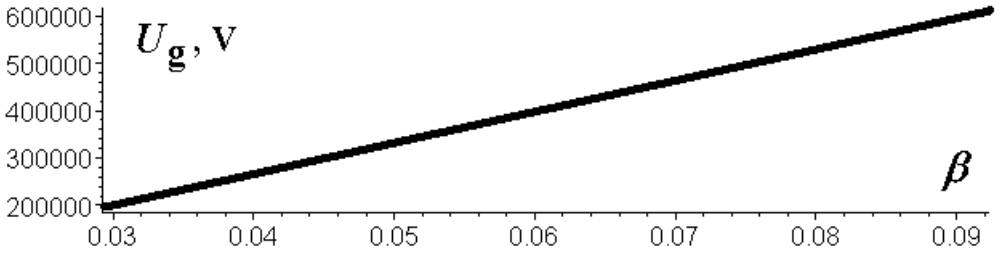

b)

Fig. 1. Voltage distribution along the APhF structure as a function of relative particle velocity: a) design with a constant voltage; b) design with a gradient voltage

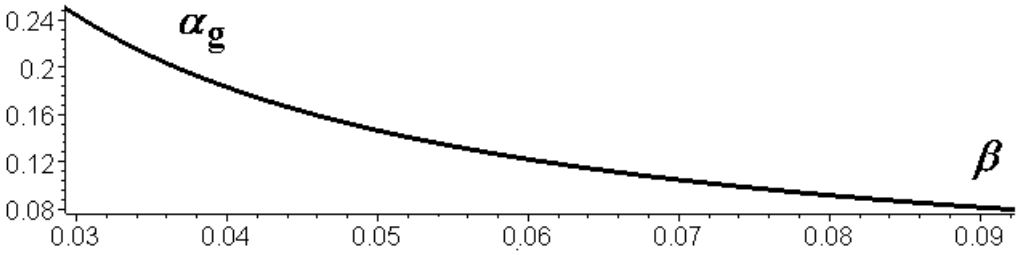

a)

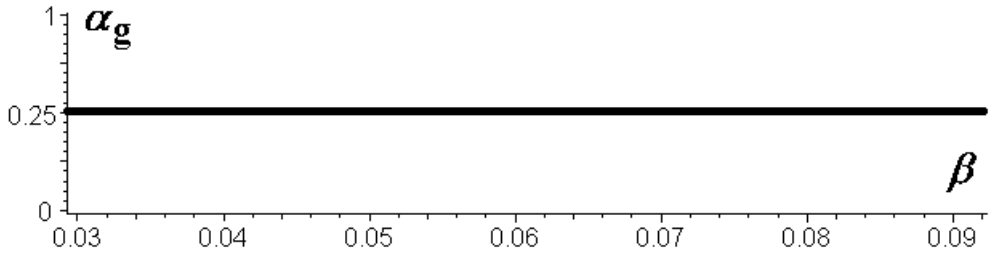

b)

Fig. 2. Distribution of the gap factor $\alpha_g = l_g / \beta_s \lambda$ along the APhF structure as a function of relative particle velocity: a) the design with a constant voltage distribution; b) the design with a gradient voltage distribution.

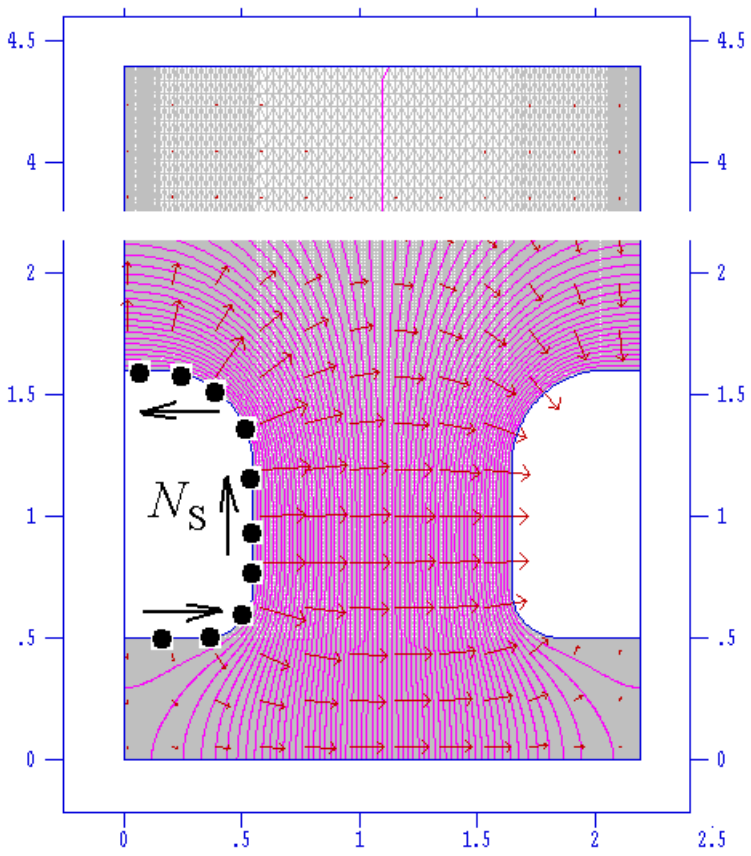

a)

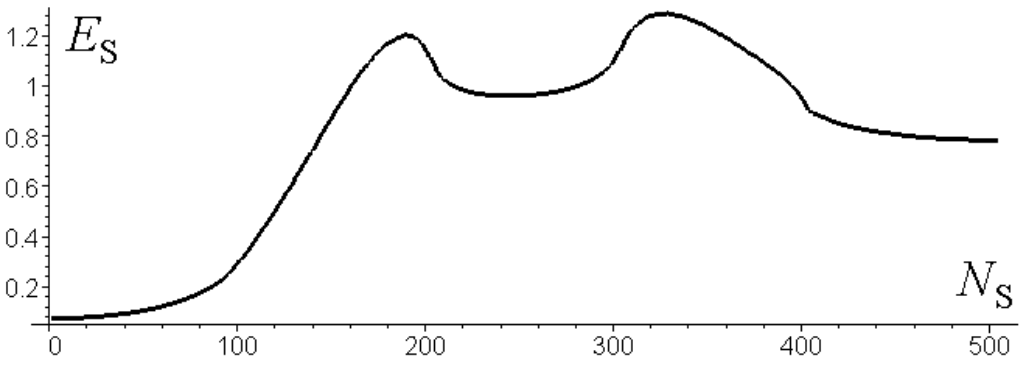

b)

Fig. 3. Electrical fields in the first accelerating cell calculated by POISSON code: a) Cross-section of accelerating cell, lines of equal potentials and electrical field arrows; b) The relative distribution of the electrical field amplitude along the surface of the left drift tube as a function of the mesh points N_S.

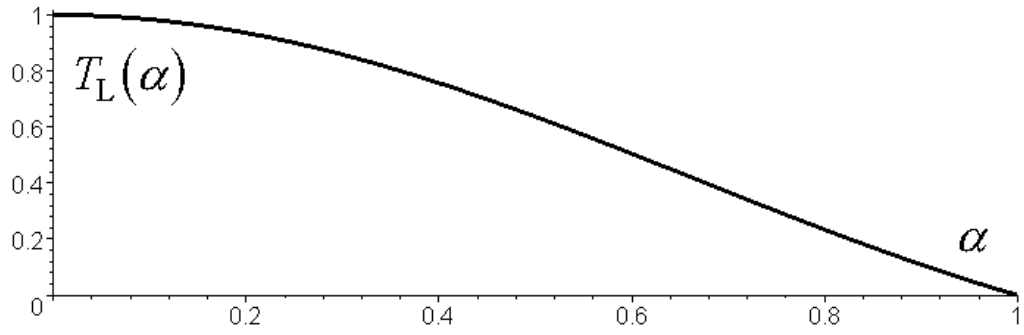

a)

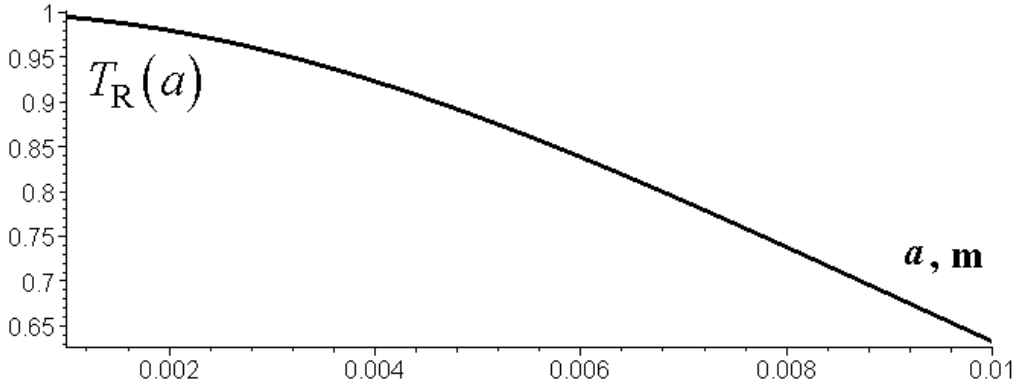

b)

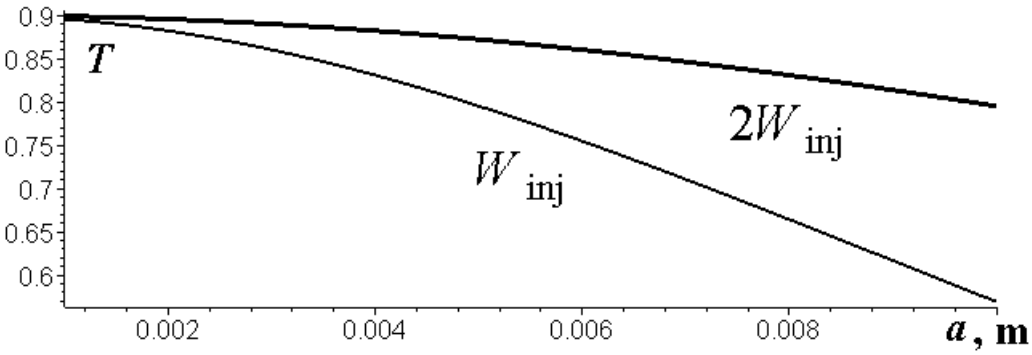

c)

Fig. 4. The dependence of transit-time-factor on the aperture radius and the gap factor: a) The dependence of the longitudinal coefficient $T_L(\alpha)$ on the gap factor, α_g at injection energy; b) The dependence of the radial coefficient $T_R(a)$ on the aperture radius, a at the injection energy W_{inj}; c) The dependence of the transit-time factor T on aperture radius at the injection energy W_{inj} and at the energy $W = 2W_{inj}$.

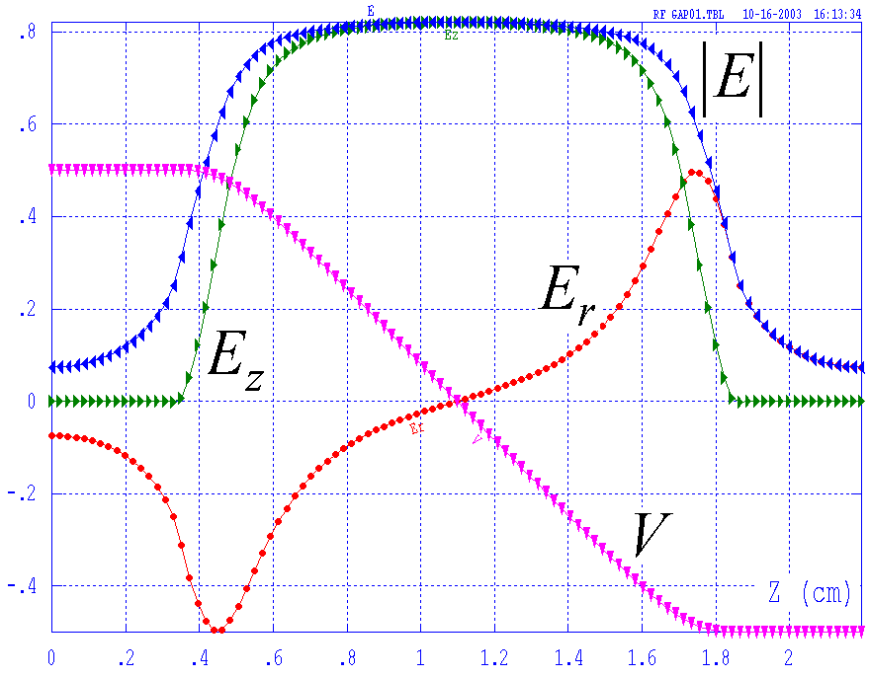

a)

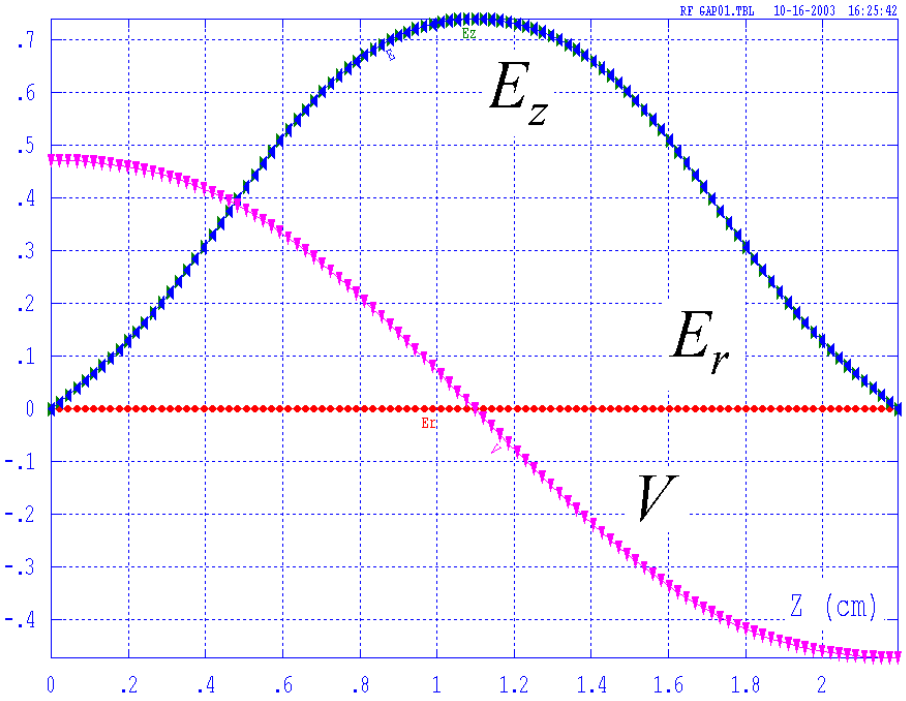

b)

Fig. 5. The potential and field distributions along the 1st accelerating cell at the injection energy: a) V, $|E|$, E_z, and E_r distributions at the aperture radius $r = a$; b) V, E_z, and E_r distributions along the cell axis $r = 0$.

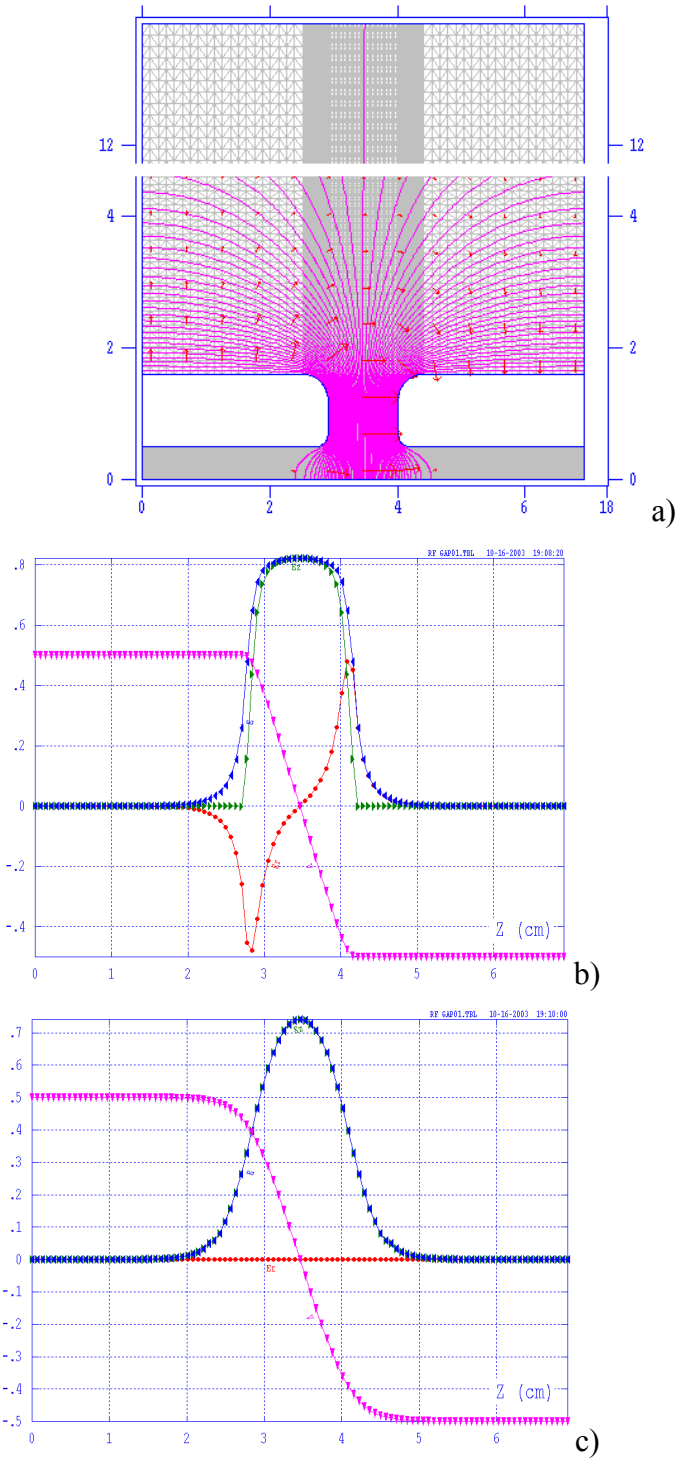

Fig. 6. Electrical fields calculated by POISSON code for the last accelerating cell of the "constant-voltage" design: a) Cross-section of accelerating cell, equipotential lines and electrical field arrows; b) V, $|E|$, E_z, and E_r distributions at the aperture radius $r = a$; c) V, E_z, and E_r distributions along the cell axis $r = 0$.

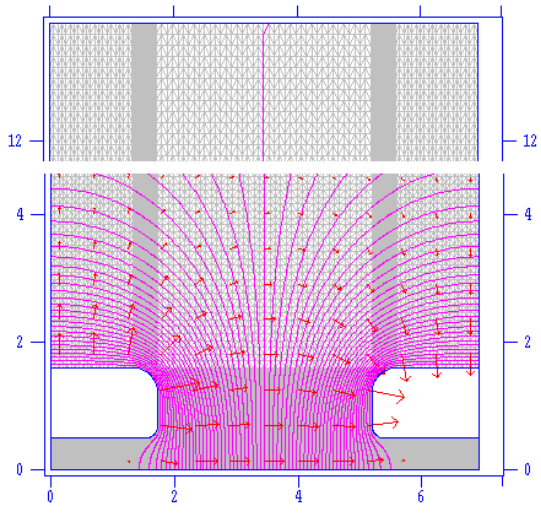

a)

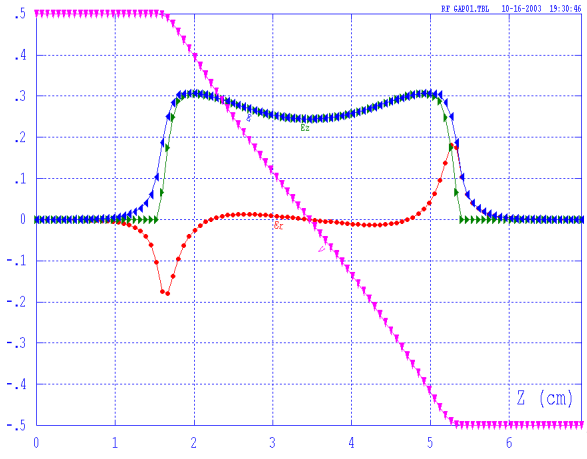

b)

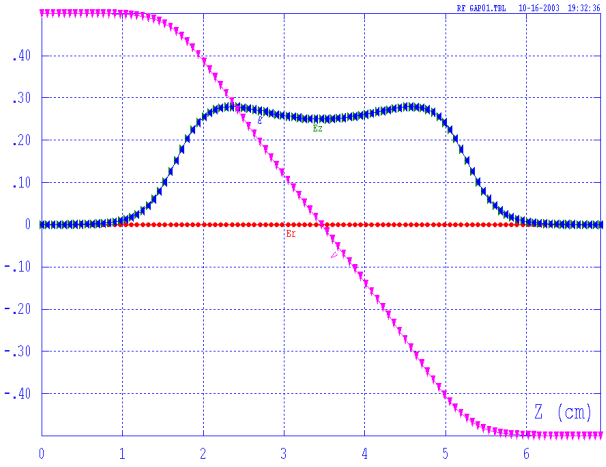

c)

Fig. 7. Electrical fields calculated by POISSON code for the last accelerating cell of the "gradient-voltage" design: a) Cross-section of accelerating cell, equipotential lines and electrical field arrows; b) V, $|E|$, E_z, and E_r distributions at the aperture radius $r = a$; c) V, E_z, and E_r distributions along the cell axis $r = 0$.

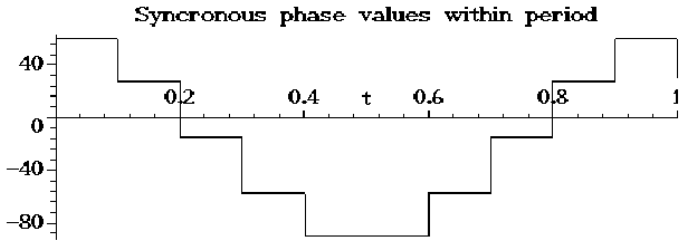

a)

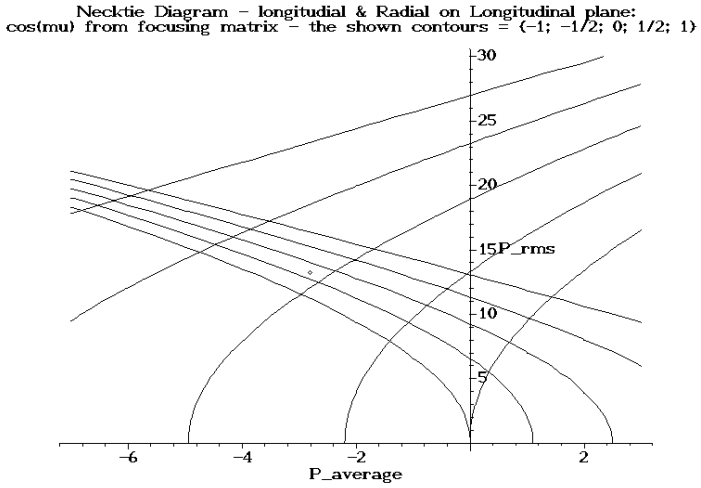

b)

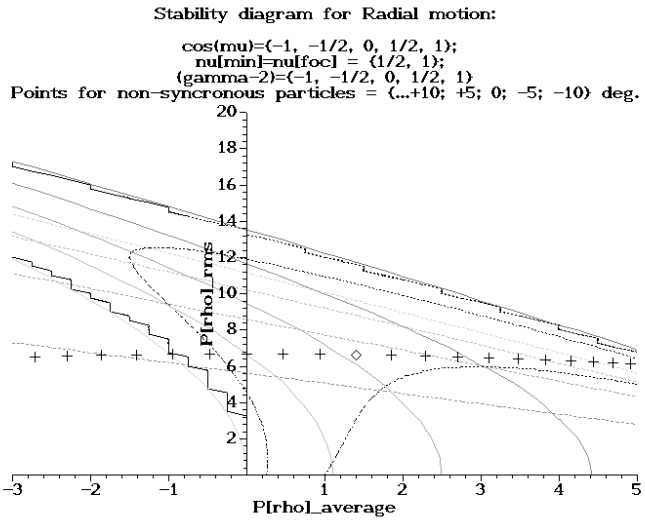

c)

Fig. 8. Stability of motion at the injection energy: a) dependence of synchronous phase within a focusing period; b) the necktie stability diagram for longitudinal and transverse motion; c) a radial stability diagram with non-synchronous particles at the injection energy.

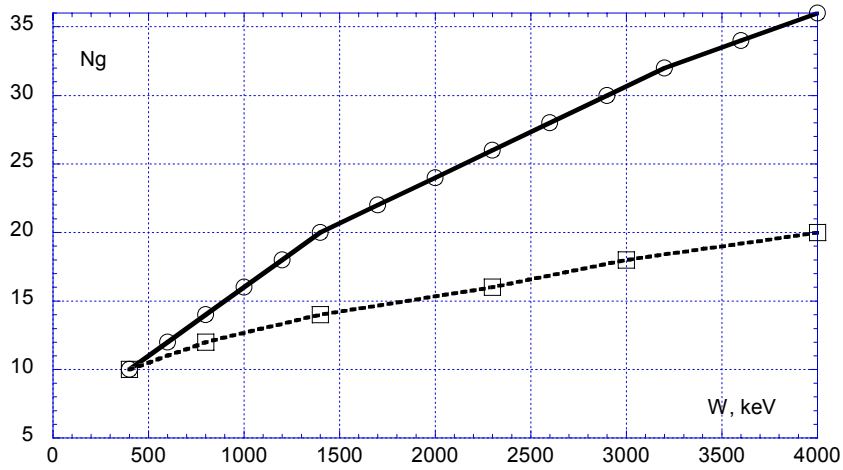

Fig. 9. The number of gaps in the focusing period N_g vs the particle energy along the whole APhF structure for the “constant-voltage” design (solid line) and for the “gradient-voltage” design (dashed line).

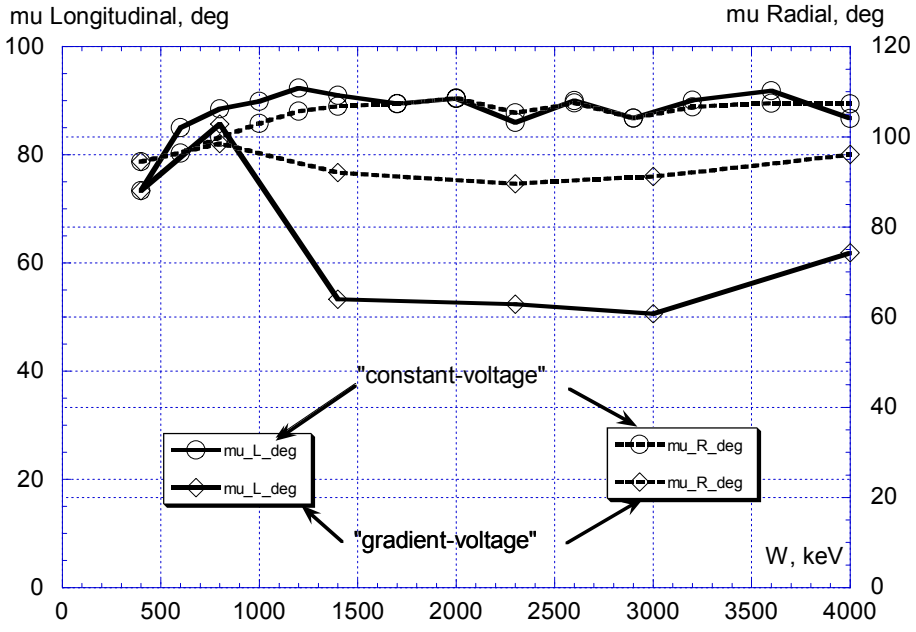

Fig. 10. The phase advances of the longitudinal (left axis, solid line) and transverse (right axis, dashed line) oscillations on the length of the focusing period for the “constant-voltage” design (circular mark) and for the “gradient-voltage” design (rhombus mark).

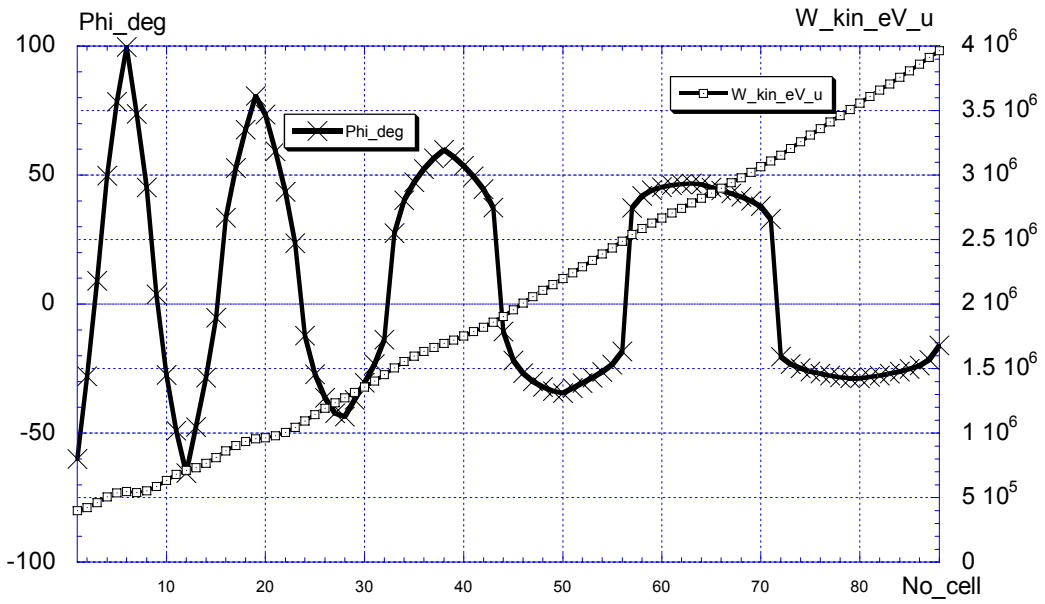

a)

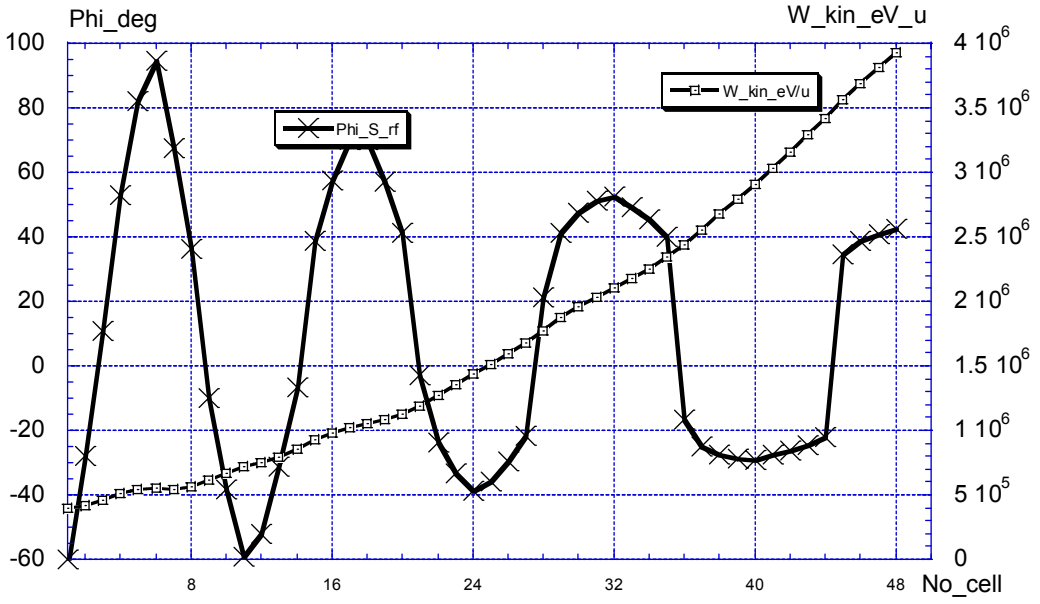

b)

Fig. 11. The synchronous phase and the reference particle energy versus the cell number for the “constant-voltage” design (a) and for the “gradient-voltage” design (b).

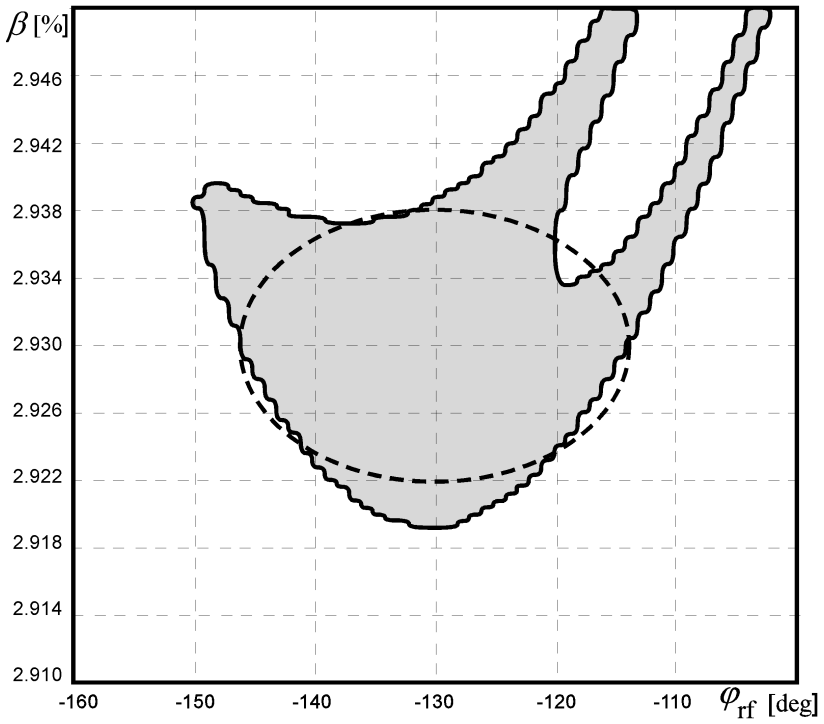

a)

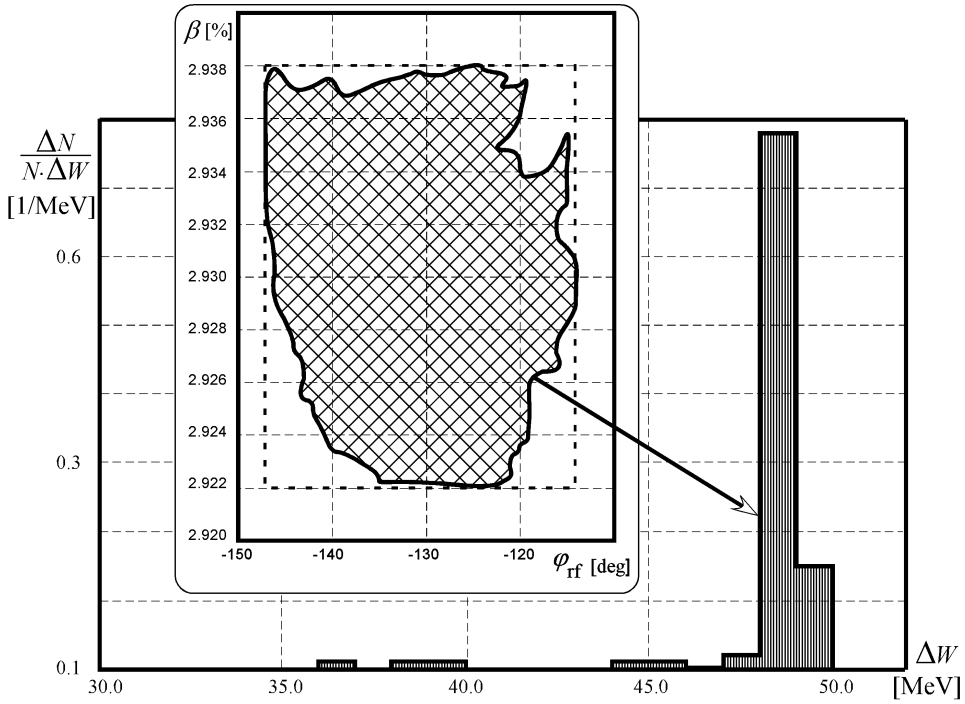

b)

Fig. 12 The longitudinal acceptance of particles moving along the axis for the "constant-voltage" design: a) the phase space area occupied by passed particles; b) the energy spectrum of passed particles.

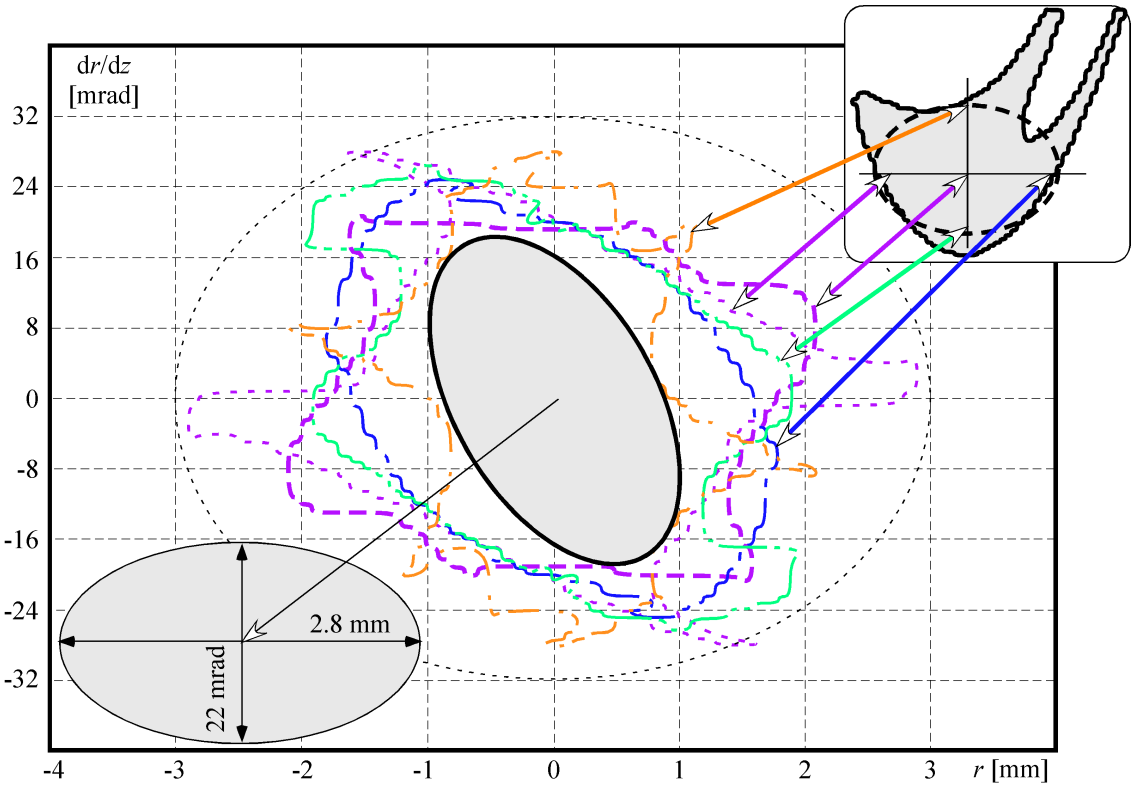

Fig. 13 Transverse particular acceptances and an effective acceptance for the "constant-voltage" design.

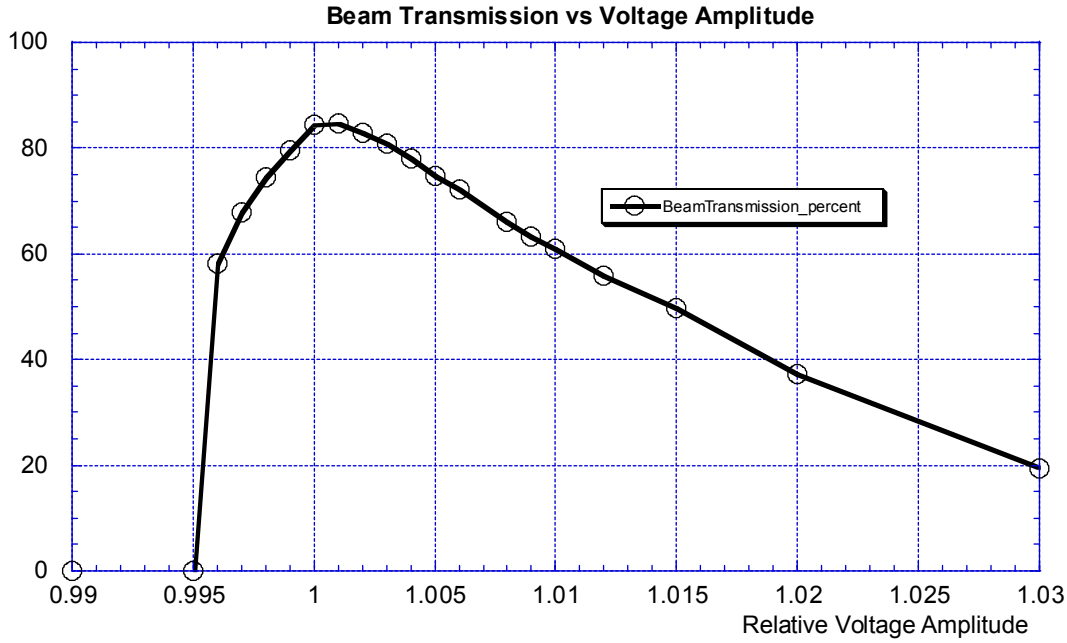

Fig. 14. The beam transmission versus the relative voltage amplitude in IH-APhF tank for the "constant-voltage" design. .

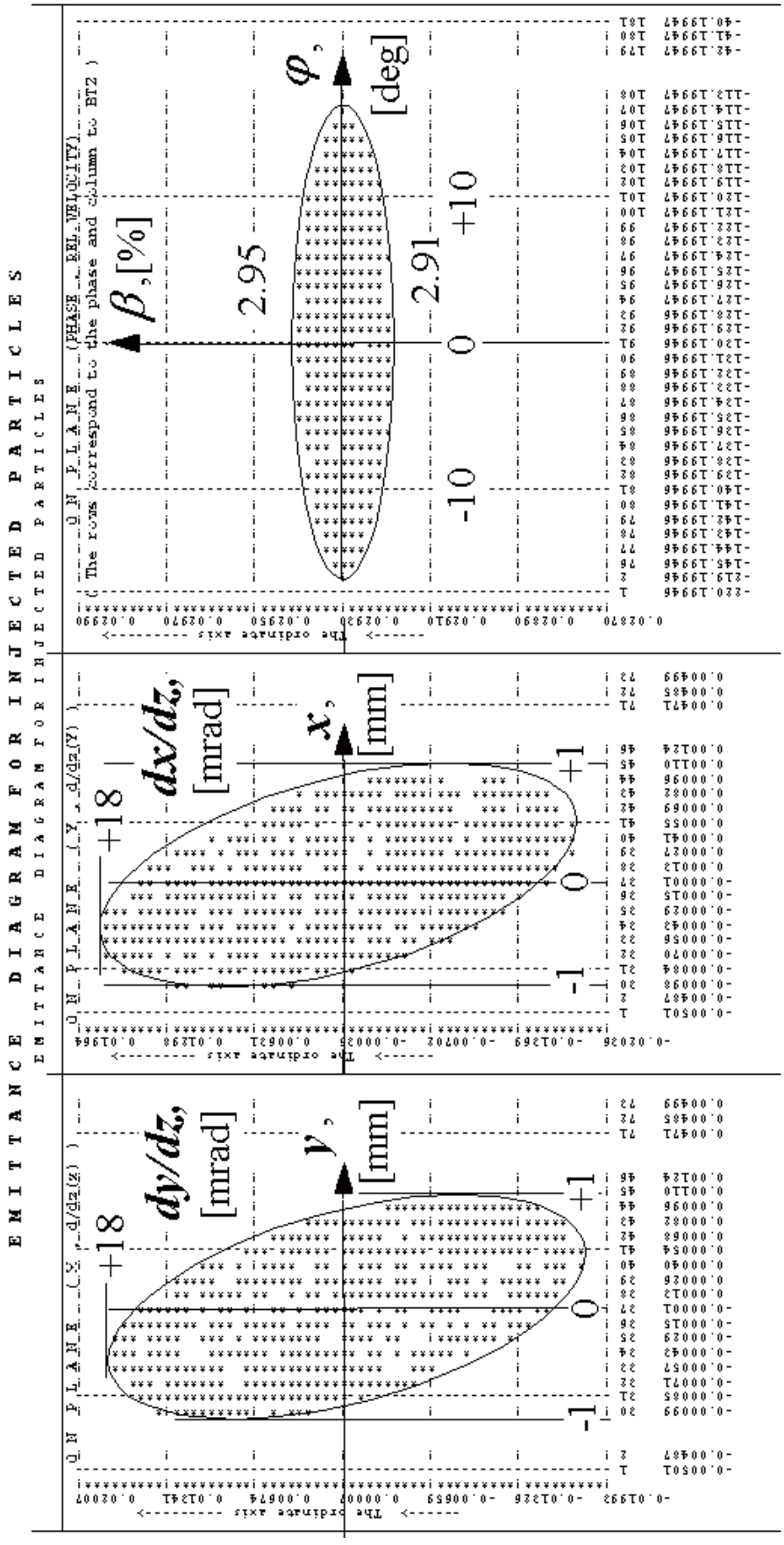

Fig. 15. The emittance of the injected beam for the “constant-voltage” design.

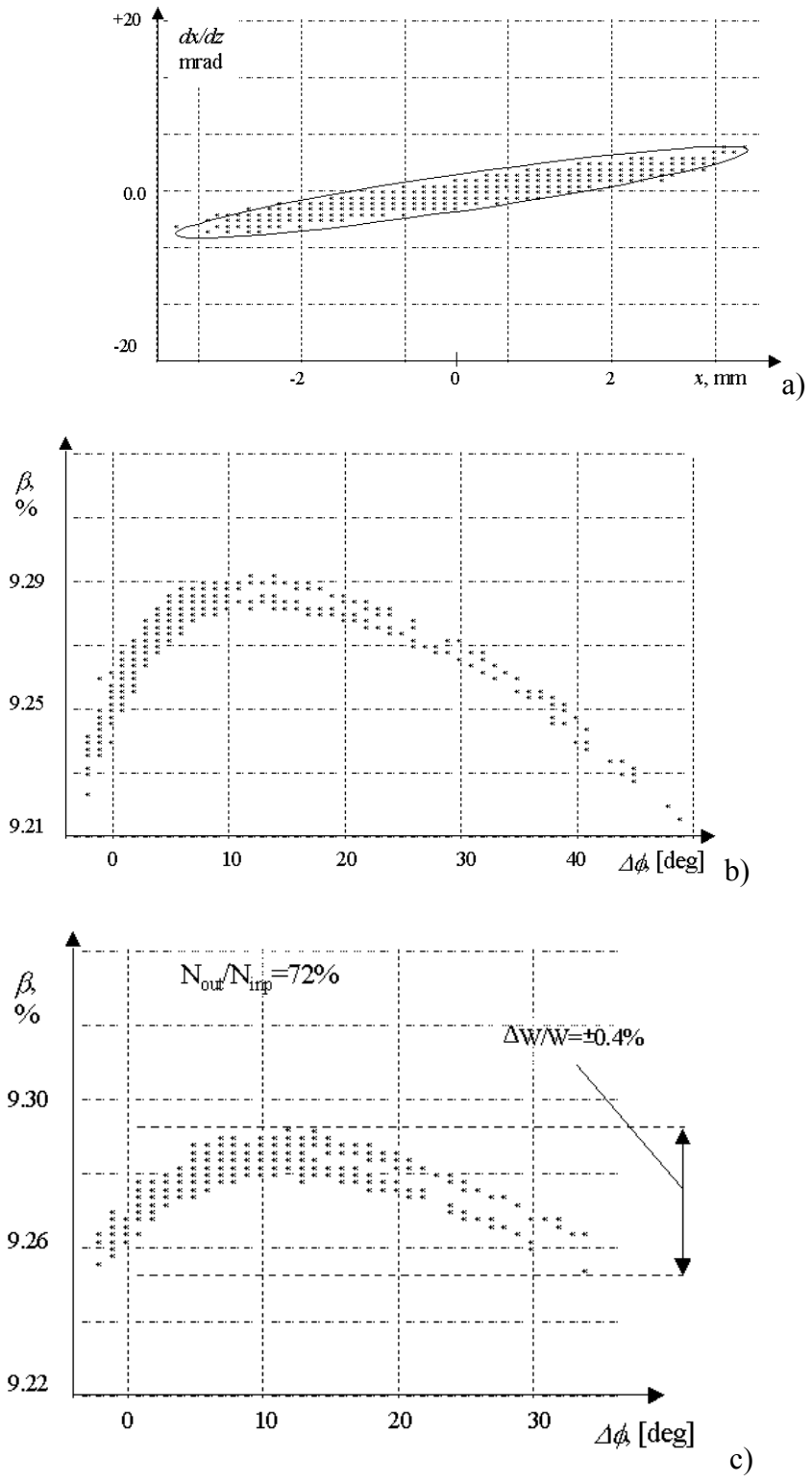

Fig. 16 The emittance of the passed particles for the "constant-voltage" design: a) the transverse emittance; b) the longitudinal emittance; c) the longitudinal emittance after a scaling of the phase law for energy spread minimization.

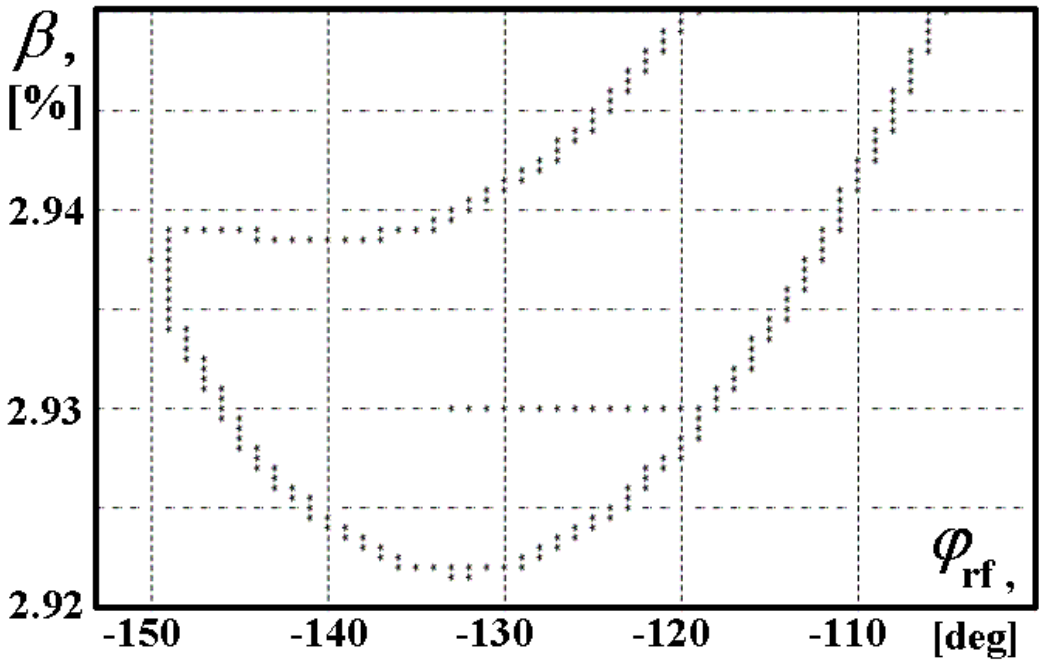

a)

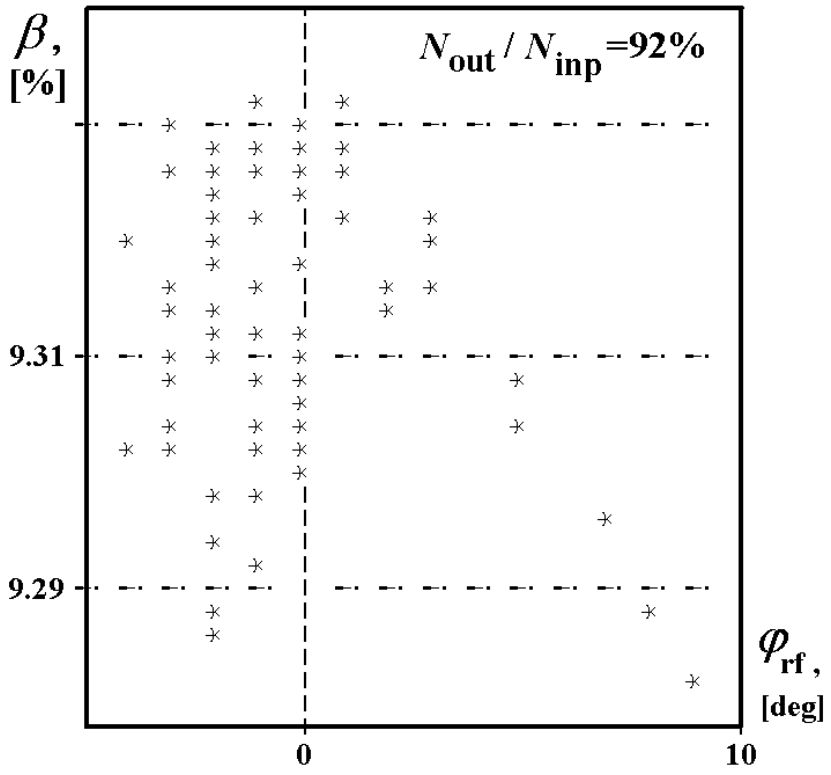

b)

Fig. 17. The longitudinal phase-space for the "gradient-voltage" design: a) the longitudinal acceptance for particles moving along the axis; b) the longitudinal emittance of the output beam for the injected beam shown in Fig. 15.

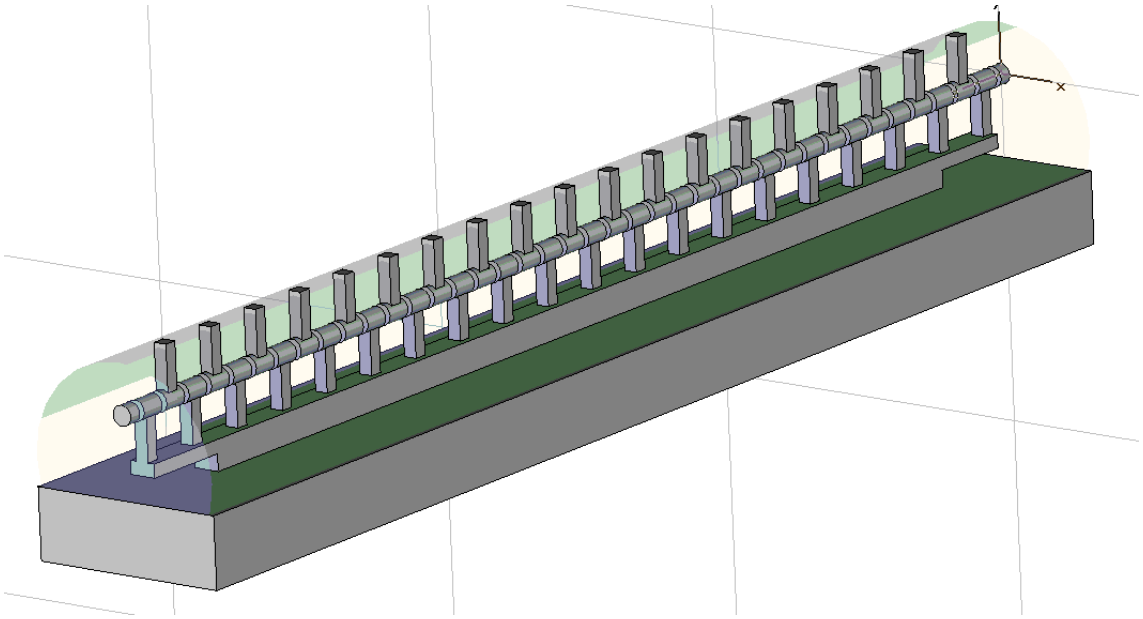

Fig. 18. The internal layout of IH-resonator with length 2 m.

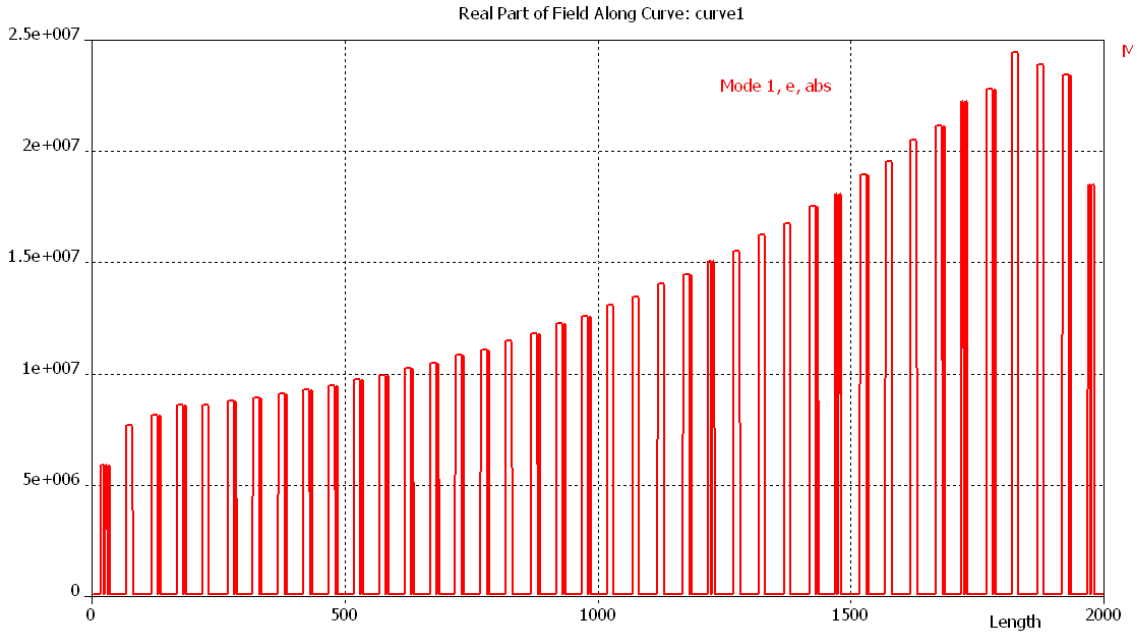

Figure 19. The voltage distribution along the IH-cavity.